Smart Electromagnetic Skin to Enhance Near Field Coverage in mm-Wave 5G Indoor Scenarios

Álvaro F. Vaquero, *Member, IEEE*, E. Martinez-de-Rioja, *Member, IEEE*, Manuel Arrebola, *Senior Member, IEEE*, Jose A. Encinar, *Life Fellow, IEEE*, Maha Achour

***Abstract*—This work proposes a Smart Electromagnetic Skin (SES) to enhance mm-wave 5G communications in indoor scenarios. The SES is based on a passive panel of reflective elements that not only redirects the impinging wave provided by the base station but also shapes the reflected field into a desired direction. The SES aims to overcome a blind zone in a coverage generated by the different propagation issues at those frequencies. The design of the SES is based on the well-known technique of the Intersection Approach for near field shaping. This fact is particularly important since the coverage in this type of scenario would have the users within the Fresnel Region of the SES and not in far-field conditions. The design goal is to generate a prescribed shaped beam in a near field area, operating in two orthogonal linear polarizations. Then, the results obtained with the synthesis techniques are used to design a reflective SES based on sets of coplanar dipoles, which provides independent control of both linear polarizations using a single-dielectric layer. As an example of interest, a pencil beam is converted into a square reflected beam of 20ºx20º. The designed SES is manufactured and measured in a planar acquisition range in order to evaluate the performance of the coverage. The measurements show a good agreement with the simulations, showing the importance of designing this type of antenna considering the radiation within the near field. The antenna operates at a central frequency of 27.60 GHz within 800 MHz, which is enough to cover two standard 5G channels.**

***Index Terms*—Smart Electromagnetic Skin, Reflective Intelligent Surface, near field, 5G mm-Wave communications.**

I. Introduction

THE USE of millimeter-wave frequency bands (such as 28 GHz, 39 GHz and 100 GHz) to provide broadband wireless access is considered as one of the leading technologies for the Fifth Generation of mobile networks (5G), as well as for future generations (Beyond 5G and 6G) [1]-[2]. The wider bandwidth available at millimeter-wave spectrum allows to deliver higher bit rates and lower latency with respect to previous generations of mobile networks (operating at sub-6 GHz frequencies) [2]-[3]. However, millimeter-wave propagation is characterized by larger path loss and penetration losses, so the signals are more sensitive to blockage by obstacles and physical barriers [4]-[5]. Therefore, the presence of these barriers (which can be high buildings, walls, furniture, or glass panels, depending on whether it is an outdoor or indoor scenario) can lead to areas with poor coverage, which are called blind zones. To extend cellular coverage in urban areas and overcome the problem of blind zones, a larger number of base stations (BS) can be deployed [6]; however, this strategy would significantly increase the costs of the network infrastructure, as well as producing higher interferences.

A low-cost and energetically efficient alternative to solve coverage problems in millimeter-wave 5G is based on the use of Reflective Intelligent Surfaces (RIS) [7]-[8]. A RIS consists of a flat surface formed by and array of reflecting cells that are designed to introduce a proper adjustment in the phase and/or amplitude of the incident wave (coming from the BS), in order to produce a reflected beam that meets the users' requirements [7]-[8]. Depending on the functionality over the reflected beam (reflecting, reconfigurability, signal amplification or signal regeneration), RIS can be classified into 4 types referred to as RIS-n [9]. RIS panels can be deployed at low cost, with low visual impact (installed on walls) and, in the case of passive RIS (also called RIS-1 [9], Smart Electromagnetic Skins [10] – SES or Klones [11]), with no energy consumption. Recent works have proposed the use of RIS in mobile networks to reflect the incident waves in a prescribed direction [12], to enhance the signal-to-interference ratio [13], to increase the energy efficiency of the network [14], to produce multiple beams for different mobile users [15], to provide a wide reflected beam

The authors would like to acknowledge Metawave Corporation for funding and leading the 5G KLONE Project. Also, this work was supported in part by MCIN/AEI/10.13039/501100011033 under grants PID2020-114172RB-C21-2 and TED2021-130650B-C22 and TED2021-131975A-I00, the last two cofounded by EU (European Union) "NextGenerationEU"/PRTR; by the Spanish Ministry of Universities and EU (NextGenerationEU/PRTR) under grant MU-21-UP2021-03071895621J; and by Comunidad de Madrid within the Multiannual Agreement Framework with Universidad Rey Juan Carlos, Line of Action 1, Young Researchers R&D Project INCREASE-5G (Ref. F858).

Álvaro F. Vaquero and Manuel Arrebola are with the Department of Electrical Engineering, Universidad de Oviedo, 33203, Gijón, Spain (e-mail: fernandezvalvaro@uniovi.es, arrebola@uniovi.es).

E. Martinez-de-Rioja is with the Department of Signal Theory and Communications and Telematic Systems and Computing, Universidad Rey Juan Carlos, 28942, Fuenlabrada, Spain (e-mail: eduardo.martinez@urjc.es)

José A. Encinar was with the Information Processing and Telecommunications Center, Universidad Politécnica de Madrid, 28040, Madrid, Spain (e-mail: jose.encinar@upm.es).

Maha Achour is with Metawave Corporation, Palo Alto, CA, USA (e-mail: maha@metawave.co).

[16], and to generate vortex modes for multiplexing schemes [17]. The previous works show the multiple benefits arising from the use of RIS at a system level; however, their practical implementation is a challenging task.

In the last years, the reflectarray technology [18] has been proposed for millimeter-wave 5G applications which include fixed and steerable beam antennas for BS and point-to-point communications [19]-[21] and terminal antennas for connected vehicles [22]. Recently, the authors have proposed the design of passive RIS (RIS-1), hereinafter referred to as SES, based on flat reflectarray panels to enhance coverage of blind zones in millimeter-wave 5G [23]-[24]. The SES proposed in those works are able to generate a reflected beam in dual-linear polarization (dual-LP) with a specific shape and pointing, which are selected to provide a proper illumination of the blind zone. The shaped coverage was accomplished by applying a phase-only synthesis (POS) technique based on the Intersection Approach algorithm [25]-[26] (note that other beamforming techniques are also possible, e.g. [27]). Compared to [23]-[24], previous implementations of coverage-enhancing printed reflectors for millimeter-wave 5G [28]-[29] only change the direction of the reflected wave without providing an optimal shaping of the beam. The SES in [23]-[24] operates within a 1 GHz bandwidth at the 28 GHz band, which is enough to cover of a pair of standard 5G channels (each around 400 MHz) [30].

The POS applied in [23]-[24] aims to achieve a shaped beam in the far field of the SES. However, it may happen that the 5G users in the blind zone are located in the near-field region of the SES panel. This is particularly likely in the case of indoor scenarios with reduced dimensions (where the blind zone can be an office or meeting room, a corridor, a staircase, and so on). In that case, the users might be located only a few meters away from the SES, while the far-field distance is around several tens of meters (depending on the electrical aperture used as SES). Thus, the beam specifications (pointing, half-power beamwidth – HPBW, etc.) might be accomplished by the near-field patterns of the SES, making it necessary the application of a near-field pattern synthesis, as in [31].

In this paper, the authors present the design, manufacturing and testing of a reflectarray-based SES (or RIS-1) to improve near-field coverage of blind zones within the $27.20 - 28$ GHz band for millimeter-wave 5G networks. The proposed SES is able to generate a shaped beam in dual-LP in the near-field region of the antenna. The results of this work demonstrate the reflectarray-based SES concept that was introduced in [23]-[24] (where no experimental validation was included, and far-field pattern synthesis was used to design the SES). The proposed SES made of a flat panel with printed elements is a low-cost and efficient solution to solve coverage problems in 5G networks, due to their simple and inexpensive fabrication (similar to the processes used for PCB fabrication), and their light weight and flat profile, which allow for a simple installation (fixed on walls or ceilings) with reduced visual impact.

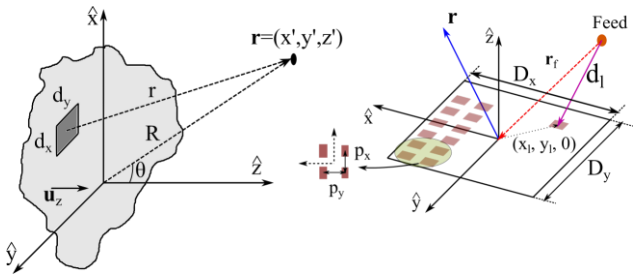

Fig. 1. Scheme of a generic planar aperture and the point of observation wherein the field is computed, and a scheme of a SES aperture and its main descriptors.

II. MM-WAVE INDOOR SCENARIO: NEAR-FIELD FORMULATION

A. *Radiated field by the SES aperture.*

Several methods exist for determining the field distribution radiated by the SES, mainly those which can be applied to aperture antennas. We take the aperture of Fig. 1 as reference, which is uniformly polarized in the direction of $\hat{x}$, and $\boldsymbol{E}_{ap}(x,y)$ is the tangential electric field on the aperture. If we consider that the SES aperture is much larger than the wavelength (λ) at the operation frequency, the radiated field can be computed as [32]

$$\boldsymbol{E}(\boldsymbol{r}) = \frac{1}{4\pi}\int_S \boldsymbol{E}_{ap}(x,y)\frac{e^{-jkr}}{\boldsymbol{r}}\left[\left(jk+\frac{1}{\boldsymbol{r}}\right)\boldsymbol{u}_z\cdot\boldsymbol{r}+jk\boldsymbol{u}_z\cdot\boldsymbol{s}\right]dxdy \quad (1)$$

where $\boldsymbol{r}$ is the vector that defines the point of observation P, R is the distance from the origin to the point of observation P, k is the free space propagation constant, $\boldsymbol{u}$ is the unit vector in the $\boldsymbol{z}$ direction, and $\boldsymbol{s}$ is the unit vector normal to the wavefront.

Concerning the distance from the aperture to P (thus r), and the size of the aperture (D), the radiated field is classified into three regions: reactive near field (if $r < 0.62\sqrt{\frac{D^3}{\lambda}}$), near field (also so-called Fresnel region) if $r < \frac{2D^2}{\lambda}$, and far field or Fraunhofer region ($r > \frac{2D^2}{\lambda}$). Depending on whether P is within the near or far field, (1) can be simplified; however, if P is in the reactive near field, (1) must be solved exactly. In the near-field case (Fresnel region), the $\frac{1}{r}$ term in brackets can be neglected when compared to k, and the $\frac{1}{r}$ term outside the brackets can be approximated by $\frac{1}{R}$. Then, $\boldsymbol{u}_z\cdot\boldsymbol{r} = \boldsymbol{u}_z$ and $R = \cos\theta$. Moreover, the variation of r over the aperture for the phase term e^{-jkr} can be approximated by the linear and quadratic terms (2)

$$r \cong z + \frac{(x-x')^2+(y-y')^2}{2z} \quad (2)$$

So that, (1) is now simplified to (3), which can be applied to compute the radiated near field in the Fresnel region.

$$\boldsymbol{E}(\boldsymbol{r}) = \frac{j}{2\lambda}\frac{e^{-jkz}}{R}\int_S \boldsymbol{E}_{ap}(x,y)e^{-jk\left(\frac{(x-x')^2+(y-y')^2}{2z}\right)}(\cos\theta + \boldsymbol{u}_z\cdot\boldsymbol{s})dxdy \quad (3)$$

From (3), it can be also derived the far-field expression, by assuming more simplifications. The phase term (2) can be

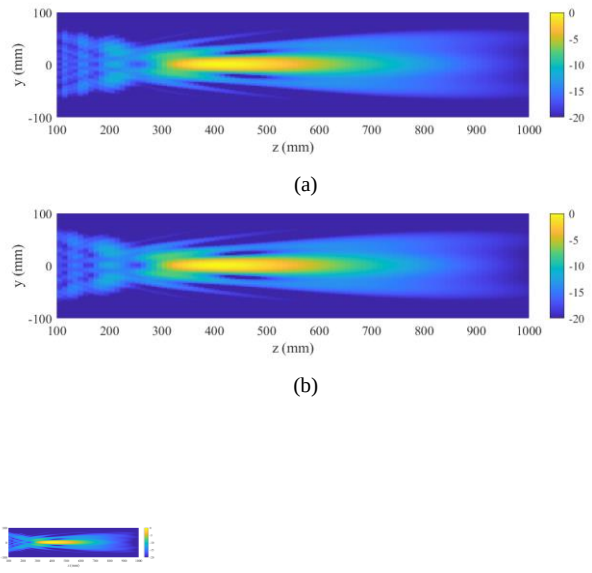

(a)

(b)

(c)

Fig. 2. Near field in the XZ plane of a focusing RIS computed through (a) Fresnel approximation (b) Principle of Superposition (c) PO/GO CST Microwave Studio at 30 GHz. The field is normalized to the maximum.

expressed as a Taylor's expansion, and the terms above the first order can be neglected [32]-[33]. For a convenience analysis, we assume that $R \to \infty$, restrict the area of observation to that near the axis z, so that $z \approx R$ and $\cos\theta \approx 1$. Under these conditions, (3) yields to the well-known expression (4) for far field. (4) is widely used in the computation of the radiated fields in antenna apertures.

$$\boldsymbol{E}(\boldsymbol{r}) = \frac{j}{\lambda}\frac{e^{-jkR}}{R}\int_S \boldsymbol{E}_{ap}(x,y)e^{-jk\sin\theta(x\cos\phi+y\sin\phi)}dxdy \qquad (4)$$

The near field expression given by (2) must yield to a valid result in the far-field region, since (4) is a further simplification. However, it is not clear whether from (4) an accurate result can be obtained when P is in the near field. Thus, applying (4) when P is in the near field might lead to unexpected results, or at least to decrease the accuracy of the results.

B. Computation of the near field: Principle of Superposition

For the computation of the near field using Eq. (3), we propose an alternative technique that simplifies the computation burden, by means of the Principle of Superposition [34].

Starting from the incident field onto a (x,y) point of the surface, the $\boldsymbol{E}_{\text{inc}}$ in both linear polarizations can be written as

$$\boldsymbol{E}^i_{\text{inc}}(x,y) = E^i_{\text{inc},x}(x,y)\hat{\boldsymbol{x}} + E^i_{\text{inc},y}(x,y)\hat{\boldsymbol{y}} \qquad (5)$$

where the superscript i denotes the polarization ($i = X$ for x-polarized incident waves, while $i = Y$ defined y-polarized wave) and the subscript the field component projected over the SES surface, so that E^X_y would be the projection of the $\hat{y}$ component when the incident field is X polarized.

Likewise, the tangential electric field reflected on the aperture can be also expressed as

$$\boldsymbol{E}^i_{\text{rlf}}(x,y) = E^i_{\text{rfl},x}(x,y)\hat{\boldsymbol{x}} + E^i_{\text{rfl},y}(x,y)\hat{\boldsymbol{y}} \qquad (6)$$

The relation between the tangential reflected and incident fields is given by the reflection matrix $\boldsymbol{R}$ (for a single element). This matrix for the (mn)-th element is given by the direct coefficients ρ_{xx} and ρ_{yy}, which mainly affects the copolar component of the radiated field; and the cross-coefficients ρ_{xy} and ρ_{yx}, which mostly affect to the cross-polar calculation. The matrix can be expressed as

$$\boldsymbol{R} = \begin{pmatrix}\rho_{xx} & \rho_{xy}\\ \rho_{yx} & \rho_{yy}\end{pmatrix} \qquad (7)$$

From the tangential reflected field $\boldsymbol{E}_{\text{rfl}}$ the near field is computed using the Principle of Superposition and the Huygens' Principle. First, the SES surface is divided into a large number of subdomains (associating each subdomain to a unit cell). Then, considering each unit-cell as a small radiating aperture, considering that the SES is comprised of many sub-apertures. Second, the near field is computed as the contribution of each subdomain at the point of observation $\boldsymbol{r}$.

$$\boldsymbol{E}_{NF}(\boldsymbol{r}) = \sum_{i=1}^{N_{SD}} \boldsymbol{E}_{SD,i}(\boldsymbol{r}) \qquad (8)$$

where N_{SD} is the number of subdomains, which is the number of unit cells of the SES; and $\boldsymbol{E}_{SD,i}$ is the radiation of the i-th subdomain at $\boldsymbol{r}$.

To compute the contribution of $\boldsymbol{E}_{SD,i}$ the classical aperture theory for planar aperture distributions can be applied. However, if the point of observation $\boldsymbol{r}$ is in the far field of the subdomain (but in the near field of the SES), $\boldsymbol{E}_{SD,i}$ can be computed under far field assumptions, which notably simplifies the complexity of the formulation. Now, the contribution of a subdomain is calculated using any of the Equivalence Principles, e.g., in [35], the First Principle of Equivalence is proposed to obtain a generalized analysis of the radiation from an SES. The approach presented in this work is based on approximating each subdomain as a small radiating aperture on a ground plane (generally smaller than $0.5\lambda \times 0.5\lambda$), allowing the use of the Second Equivalence Principle [36], simplifying the analysis to only consider the tangential electrical field (see Appendix).

C. Comparison between models

In this section, the accuracy of the Principle of Superposition is compared with the Fresnel equation, as well as a combined geometric optics and physic optics (PO-GO) analysis through CST Microwave Studio [37]. To do so, the near field of a near-field focusing RIS of $20\lambda \times 20\lambda$ (200 mm × 200 mm) is computed at 30 GHz. We consider a regular distribution of the elements with a periodicity of $0.25\lambda_0$ ($p_x = p_y$) in both x- and y- direction, according to the coordinate system shown in Fig. 1. Then, the tangential field for a linear-polarized electric field is defined as:

$$\boldsymbol{E}_{ap}(x,y) = E_0 e^{jk_0\frac{(x^2+y^2)}{2F}}\hat{\boldsymbol{x}} \qquad (9)$$

where F is the focusing point, in this case $(x',y',z') = (0,0,450)$ mm; and E_0 is the amplitude of the tangential field, which is a uniform illumination ($E_0 = 1$).

To facilitate comparison, the development of (3) and (4) for the focusing case is detailed in Appendix I and Appendix II, respectively. For this case, the near field is computed in the transversal plane XZ, which is shown in Fig. 2.

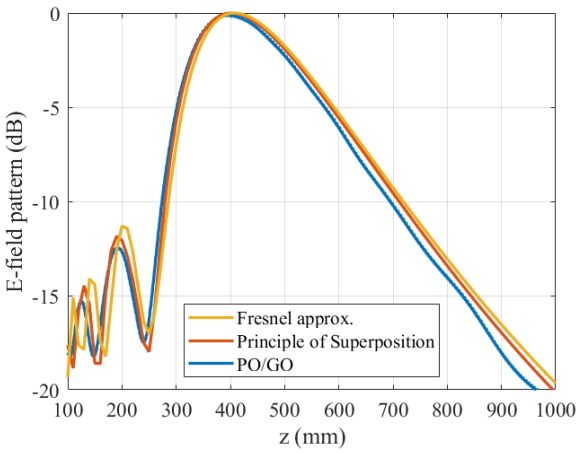

Fig. 3. Comparison of the near field in the cut $y = 0$ computed through: Fresnel approximation, Principle of Superposition and PO/GO CST Microwave Studio at 30 GHz. The field is normalized to the maximum.

Fig. 2 shows the near field computed with Fresnel approximation (eq. (3)), Principle of Superposition (eq. (8)) and PO-GO from CST Microwave Results. Moreover, Fig. 3 shows a comparison of the three models for the cut $x = 0$ and $y = 0$, which is the cut containing the focused spot. As can be observed, all three calculation methods offer similar results throughout the entire calculation domain. In Fig. 3, the cut containing the focused spot ($y = 0$) is compared, showing a high agreement among the models used. Therefore, the Principle of Superposition, despite modeling the contribution of a subdomain with far-field formulation, provides similar results while reducing the complexity of the calculation. It should be noted that the resolution of the Fresnel equation (3) involves the use of Fresnel integrals, which do not have analytical resolution and require the use of tables or numerical methods, where convergence may limit the accuracy of the resolution reached.

III. Synthesis to Enhanced the Near-Field mm-Wave Coverage

The Smart Electromagnetic Skin is synthesized using the Intersection Approach (IA). Broadly speaking, the IA searches for the intersection of two sets, or at least, the minimal distance between both [38]. The IA defines the set $\mathcal{M}$, which gathers the radiated field that comply the requirements, and the set $\mathcal{R}$, which gathers the fields that can be radiated by the antenna geometry. The intersection of both sets is searched by means of Alternate Projections. Mainly, in each iteration the IA performs the double operation defined as $\boldsymbol{E}_{NF}^{i+1} = \mathcal{B}\left[\mathcal{F}\left(\boldsymbol{E}_{NF}^{i}\right)\right]$. This operation requires to define the forward projector $\mathcal{F}$, and the backward projector $\mathcal{B}$. Then, $\boldsymbol{E}_{NF}$ is the field radiated by the SES in the ith-iteration. $\mathcal{F}$ projects a point of $\mathcal{R}$ onto $\mathcal{M}$, while $\mathcal{B}$ retrieves a point of $\mathcal{M}$ onto $\mathcal{R}$.

The IA ideally aims to find a field that belongs to both sets, therefore a field that can be radiated by the antenna geometry and satisfies the requirements (if that is not possible, at least finding a field whose distance to $\mathcal{M}$ is minimal). Starting from the field at the aperture of the SES ($\boldsymbol{E}_{\text{rfl}}(x,y)$ (6)) the radiated field can be computed by using (8), being $\boldsymbol{E}_{NF}(\boldsymbol{r})$ a radiated field in the near field that belongs to $\mathcal{R}$. Then, $\mathcal{F}$ projects $\boldsymbol{E}_{NF}(\boldsymbol{r})$ onto $\widetilde{\boldsymbol{E}}_{NF}$ (which belongs to $\mathcal{M}$) by means of applying the condition $U_{lwr} \leq \widetilde{\boldsymbol{E}}_{NF} \leq U_{upr}$ (where U_{lwr} and U_{upr} are the lower and upper boundaries of the constraints, respectively). Then, $\mathcal{B}$ retrieves the tangential field $\widetilde{\boldsymbol{E}}_{\text{rfl}}(x,y)$ that generates a field on $\mathcal{M}$ but cannot be implemented by the antenna, therefore other constraints might be applied. This process is iterated until finding the intersection.

In the classical implementation of the IA, as well as other alternate-projection-based methods, the projectors are implemented by a direct-inverse operator, such as the FFT/IFFT [39], [40]. However, this implementation limits the region wherein the constraints are imposed to planes parallel to the antenna aperture. The implementation used in this work is based on the generalization of the Intersection Approach, particularly for near-field synthesis [41]. In this case, the projector $\mathcal{B}$ is implemented by means of an optimization algorithm instead of the FFT, so the constraints are imposed in arbitrary planes. In this case, the $\mathcal{B}$ is implemented through the Levenberg Marquardt Algorithm (LM).

In direct optimization methods (the one used to implement $\mathcal{B}$), a functional d is defined as an error cost function to be minimized. This functional is commonly used to evaluate the distance between $\boldsymbol{E}_{NF}^{DO}(\boldsymbol{r})$ (which is a field radiated by the antenna and belongs to $\mathcal{R}$, this field is computed within the optimization algorithm) and $\widetilde{\boldsymbol{E}}_{NF}$. The functional d is commonly defined by using the Euclidean distance. However, the functional d is enhanced by the System-by-Design Paradigm [42]. This Paradigm is based on the inclusion of a particular figure of merit in the evaluation of the error, which improves the convergence of the algorithm [43]:

$$d(\boldsymbol{r}) = \int_{\Omega} \left\{ \delta \left(\left|\widetilde{\boldsymbol{E}}_{NF}(\boldsymbol{r})\right|^2 - \left|\boldsymbol{E}_{NF}^{DO}(\boldsymbol{r})\right|^2 \right) + \delta' \left(R_p' - R_p^{LMA}(\boldsymbol{r})\right) + \delta'' \left(S_{LL}' - S_{LL}^{LMA}(\boldsymbol{r})\right) \right\} d\Omega \tag{10}$$

where Ω is the integration domain; $\boldsymbol{r}$ is the point wherein the field is evaluated; $\widetilde{\boldsymbol{E}}_{NF}(\boldsymbol{r})$ is the radiated field after applying the forward projector $\mathcal{F}$, and $\boldsymbol{E}_{NF}^{DO}(\boldsymbol{r})$ is the field used by the direct optimization algorithm to evaluate the functional d. $\boldsymbol{E}_{NF}^{DO}(\boldsymbol{r})$ is related with the field at the aperture of the SES ($\boldsymbol{E}_{\text{rfl}}(x,y)$) as $\text{FP}\left(\boldsymbol{E}_{\text{rfl}}^{DO}(x,y)\right)$, being FP$(\cdot)$ the forward propagation model defined by (8). R_p' and S_{LL}' are the reference parameters of the ripple within the coverage and the SLL of the field pattern, respectively. Whereas R_p^{LMA} and S_{LL}^{LMA} are the same parameters but evaluated in the current $\boldsymbol{E}_{NF}^{LMA}$. δ, δ' and δ'' are a weighting function that depend on the observation point, and they balance the weight function among the different figure of merits.

The ripple R_p and the S_{LL} are defined as

$$R_p(\boldsymbol{r}') = \max\{\boldsymbol{E}_{NF}(\boldsymbol{r}')\} - \min\{\boldsymbol{E}_{NF}(\boldsymbol{r}')\} \tag{11}$$

$$S_{LL}(\boldsymbol{r}'') = \max\{\boldsymbol{E}_{NF}(\boldsymbol{r}'')\} - \max\{\boldsymbol{E}_{NF}(\boldsymbol{r}'')\} \tag{12}$$

where $\boldsymbol{r}'$ is the point of observation defined within the coverage and $\boldsymbol{r}''$ a point of observation defined outside the coverage.

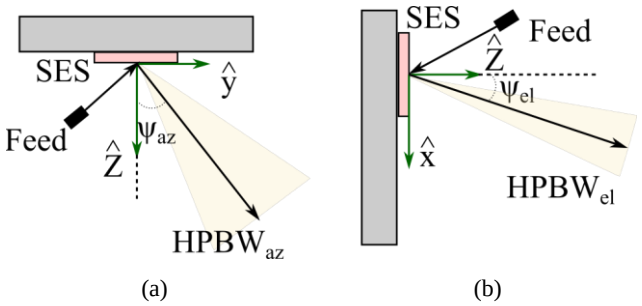

(a) (b)

Fig. 4 (a) Azimuth and (b) elevation views of the indoor scenario, with the SES fixed on the wall (the *z*-axis is normal to its surface), showing the beam requirements of the SES.

IV. Smart Electromagnetic Skin for Near Field Coverage: Near- and Far-Field Design

A. Antenna geometry and scenario definition

The SES has a rectangular shape, and its dimensions are $400\ \text{mm} \times 400\ \text{mm}$. The central operating frequency of the SES is 27.6 GHz, and a bandwidth requirement of 800 MHz has been considered to ensure that the SES can operate over two 5G channels of 400 MHz each. A conventional indoor scenario is considered to deploy the proposed SES, which will be installed in the wall. The feeder is a BS located far from the SES at $(x, y, z) = (-1.26, -5.64, 15.49)\ \text{m}$, considering the reference coordinate system of Fig. 4. The feeder is modeled using a $\cos^{\text{q}}\theta$ function with a q-factor of 56, which provides a uniform field distribution along the SES surface.

The electric requirements of the SES to ensure a proper coverage of the blind zone in the indoor scenario are as follows: the reflected beam in dual-LP must point at $\psi_{az} = 30°$ in azimuth and $\psi_{el} = 0°$ in elevation (see Fig. 5). Note that, the input angles from the feeder (with respect to the geometric center of the SES) are $-20°$ in azimuth and 4.65° in elevation, so the SES must be designed to generate the reflected beam at a different direction from the specular one (which would be $\psi_{az} = 20°$ and $\psi_{el} = -4.95°$). Moreover, if a $400\ \text{mm} \times 400\ \text{mm}$ reflective panel is designed to produce a pencil beam, it would provide only around 2° HPBW coverage in both elevation and azimuth planes. Thus, the SES panel must be designed to both redirect and broaden the dual-LP reflected beam 10° in both elevation (HPBW_{el}) and azimuth (HPBW_{az}) to comply with the scenario specifications. For this purpose, a pattern synthesis process will be carried out to reach a shaped beam with the required pointing and HPBW.

The key point of the SES design is that the blind zone is located at a distance around 12 m from the SES. According to the operating frequency (27.6 GHz) and SES size ($0.4\ \text{m} \times 0.4\ \text{m}$), the 5G users in the blind zone are located in the near-field region of the SES. Therefore, far-field radiation patterns cannot be used to properly characterize the SES performance in the indoor scenario. The beam requirements (pointing, HPBW, and so on) must be accomplished in the near-field pattern of the SES, so the pattern synthesis must be conducted in near field (as explained in Section II and following the procedure described in Section III), unlike previous SES designs where farf-field pattern synthesis was conducted [23]-[24].

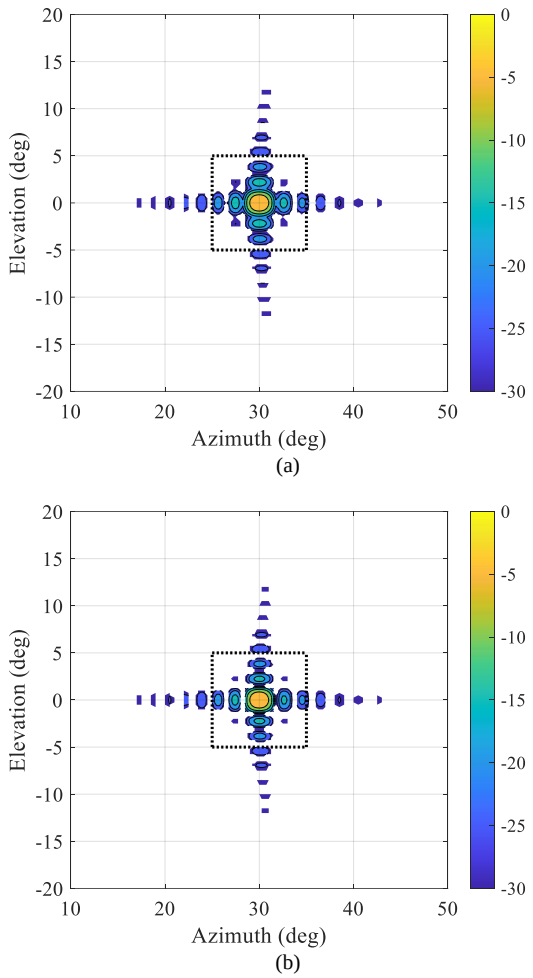

Fig. 5. Near-field pattern (dB) radiated by the phase distribution computed with (13) (a) at 12 m and (b) in the far-field region. The field is normalized to the maximum of the coverage area and the dotted black lines are the coverage boundaries.

B. Near- and far-field Phase-Only Synthesis

To highlight the importance of designing the SES considering that the user is within the near-field region and not using a far-field SES analysis, two designs are carried out for the described scenario. One design is conducted by imposing the desired conditions at the required distance of 12 m (near-field), and the second design assuming far-field conditions, in order to evaluate the differences between them. Note that, the blind zone is always at 12 m.

The first design approach is to use the phase-shift distribution of a collimated beam in the direction (ψ_{el}, ψ_{az}), which are the outgoing angles pointing to the center of the coverage. This approach is analytically computed as follows [18]:

$$\phi_l^i(x_l, y_l) = k_0(d_l - (x_l \cos\varphi_b + y_l \sin\varphi_b)\sin\theta_b) \qquad (13)$$

where d_l is the distance from the base station to the lth element, k_0 is the wavenumber in vacuum, and the superscript denotes the polarization of the feed according to the system of coordinates shown in Fig. 2 (V-pol is oriented according to the x-axis, while H-pol is oriented to the y-axis). In this case, two phase-shift distributions are computed, one for each linear

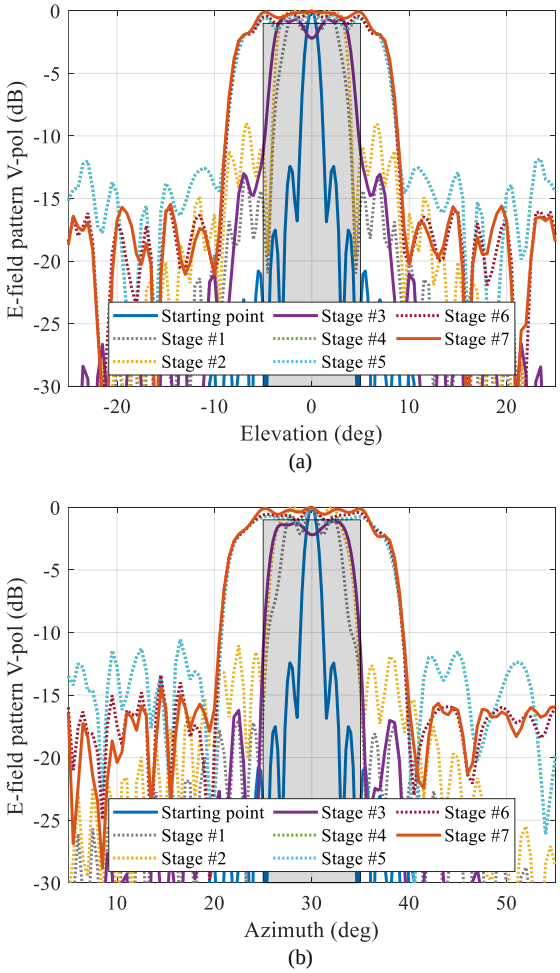

Fig. 6. Comparison of the near-field pattern before, after and during the POS performed for (a) elevation and (b) azimuth cuts at 27.6 GHz. The field is computed at 12 m.

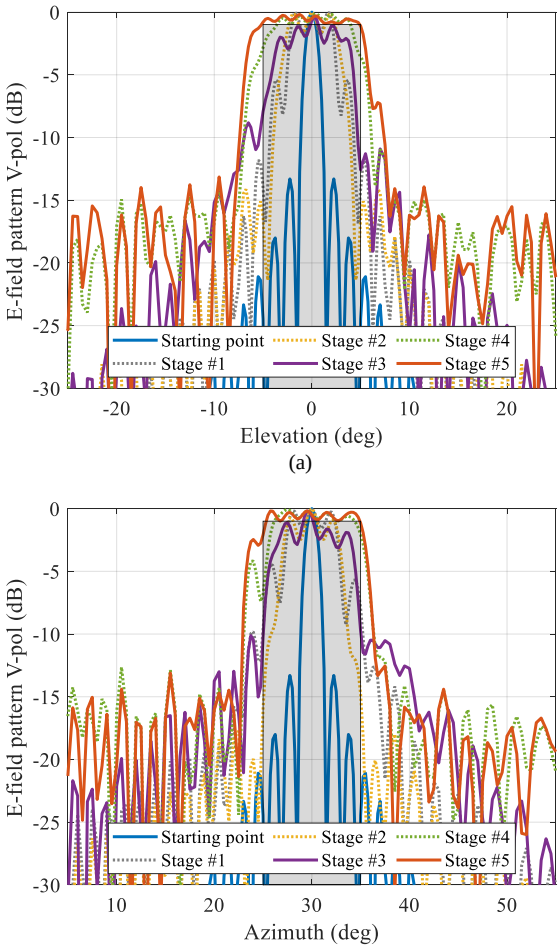

Fig. 7. Comparison of the far-field pattern before, after and during the POS performed for (a) elevation and (b) azimuth cuts at 27.6 GHz.

Table I. Outline of the iterations and constraints of the Intersection Approach required in each stage of the near-field multi-stage procedure.

Stage	1	2	3	4	5	6	7	TOTAL
# it.	149	787	123	48	2620	892	1573	6192
Ripple	3	2.5	2	2	2	1.5	1	1
HPBW	5	6.50	6.50	8	10	10	10	10

Table II. Outline of the iterations and constraints of the Intersection Approach required in each stage of the far-field multi-stage procedure.

Stage	1	2	3	4	5	TOTAL
# it.	924	14	703	4600	4600	10841
Ripple	3	2.5	2	1.5	1	1
HPBW	5	5	7	8.5	10	10

orthogonal polarization. (θ_b, φ_b) are the angles associated with the center of the coverage in spherical coordinates.

The phase-shift distribution given by (13) collimates a beam with the highest gain at (ψ_{el}, ψ_{az}) for the aperture used, which is desirable to enhance the signal level. However, the coverage angular range is quite short to cover the blind area. The HPWB of the pencil beam is about 2°, while the coverage requires 10 by 10 degrees. Fig. 3(a) shows the near-field pattern at 12 m obtained with the phase-shift distribution of (12), and Fig. 3(b) shows the far-field pattern, in both cases resulting in a very well-collimated beam. Hence, according to the scenario requirements, the beam must be broadened in both elevation and azimuth.

To do so, two POS processes are carried out, one for each linear polarization, since POS cannot deal with two polarizations simultaneously. These POS are carried out twice, one considers near field constraints, and the others far field constraints, so a total of 4 POS are performed. However, the process is simplifier to only 2 POS since it is assumed that both linear polarizations introduce the same phase-shift distribution (only the V-pol POS is carried out). Each of the POS is based on the Intersection Approach with the enhanced functional introduced in Section III. In all cases, the starting point of the POS is the phase-shift distribution of (13). The synthesis aims to broaden the field pattern to cover the required angular specifications while the field distribution is uniformized (with a ripple lower than 1 dB) within this area. It is worth noting the complexity of the synthesis due to the tight requirements needed. The beam in azimuth must be broaden over 10° using a starting point with a HPBW of about 2°. Moreover, in the coverage area the pencil beam generates several nulls that must be filled to reach a uniform field distribution. The syntheses have been addresses with the same process, following a multistage strategy [41],[43]. In this type of strategies, the

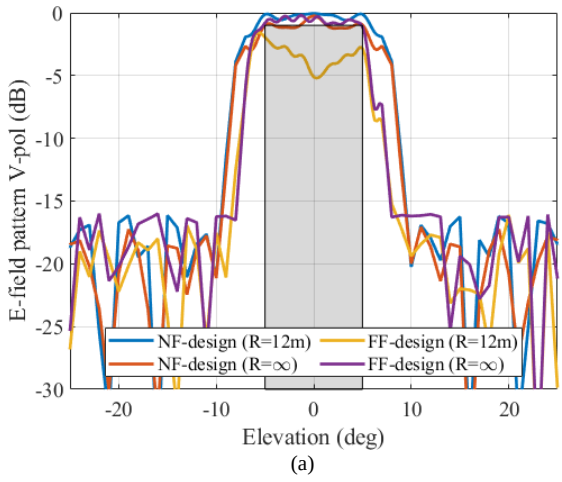

(a)

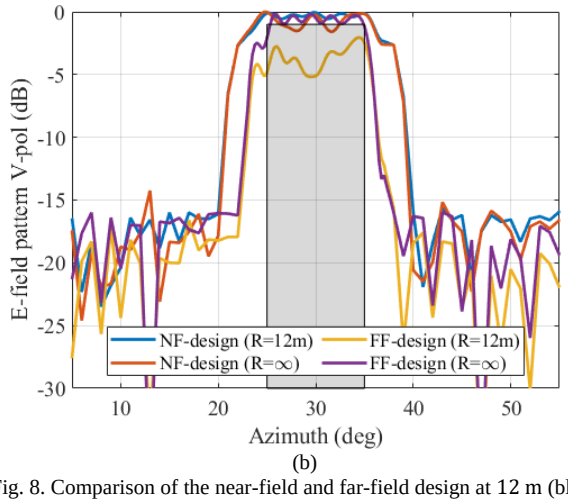

(b)

Fig. 8. Comparison of the near-field and far-field design at 12 m (blind zone) and far field, for the two designs at 27.6 GHz and V-pol. (a) Elevation (b) Azimuth cuts.

synthesis process is divided into different sub-synthesis whose goal is to reach an intermediate result. This fact allows to improve the starting point from one sub-synthesis to the other, while the specifications are gradually tightened in each new sub-synthesis until finally reaching the desired requirements [41]. This point is especially important in local optimization algorithms, as a multi-stage procedure not only allows reaching solutions that are far from the starting point but also enhance convergence by minimizing the risk of falling into traps or local minima. The price to pay is the subdivision of a single-stage synthesis into multiple syntheses, increasing the computational cost of the entire process. However, in a single-stage approach, reaching or approximating the desired solution is not guaranteed [41], and computational efficiency can be significantly improved in the near field with the use of speed-up techniques such as Differential Finite Contributions (DFC) on the gradient computation [44]. Generally, in the first steps the goal is to slowly broaden the beam, preserving a low ripple, while the latest stage goal is to refine the ripple and decrease the sidelobe level (see Fig. 6 and Fig. 7).

Table I outlines the information of the multi-stage performed with near-field constraints until reaching the desired solution. A total of 7 stages (sub-syntheses) were required and for each

Table III. Comparison of the compliance of the near-field and far-field design evaluated in the coverage at the blind zone distance and far field.

Design	Distance	1 dB (%)	Mean Ripple*	Ripple coverage**	Mean error***
NF	12 m	100	0.29	0.29	0
NF	∞	55.29	0.95	1.46	0.75
FF	12 m	7.95	0.63	2.60	1.77
FF	∞	93.81	0.54	0.58	0.58

*Mean ripple of the field within 1-dB compliance.
**Mean ripple within the angular range of the coverage.
***Mean error of the field outside the compliance and 1-dB ripple.

stage several iterations of the Intersection Approach are needed (6192 in total) for the V-pol were required. Then, for each iteration of the Intersection Approach the only 3 iterations of the LM are required [39].

The output of the synthesis is the phase-shift distribution of the SES elements that radiates the near-field pattern that meets the coverage specifications. Fig. 6 shows the main elevation and azimuth cuts at the central frequency, for the starting and final point, and the intermediate solutions reached for the V-pol. A major improvement is reached in both directions, successfully covering the entire angular range. The starting point (pencil beam) has been broadened more than 8° in both directions, maintaining a very low ripple, lower than 1 dB and an average ripple of 0.29 dB. The compliance of the specification goes up from 0.59% to a 100%, so that both results totally meet the specifications.

Following the same procedure for the two syntheses with far-field constraints, a total of 6 stage were required with the iterations of the Intersection Approach shown in Table II. Fig. 7 shows the main elevation and azimuth cuts for the starting and final point, and the intermediate point. Starting from nearly the same pencil beam (only the SLL slight changes with distance), the POS achieves to broad the beam the 10° required in both directions. The compliance increases from 0.59% to a 93.81%, almost satisfying the requirements in the entire angular range. The ripple is nearly preserved below 1 dB with a mean value of 0.54 dB, and the mean error is below 0.5 dB (for a 1.5 dB criteria the compliance increases up to 99.9%). Similar results are reached for the H-pol.

Considering these results in terms of compliance, ripple and angular range, either far- or near-field designs can be used. However, only the near-field design considers the real distance to the blind zone, thus the fact that is near-field region. Now, the results obtained for the near-field design is evaluated at far-field, while the far-field design is evaluated at 12 m (near field) to evaluate potential differences. Fig. 8 compares the main cuts of the coverage obtained when both designs are evaluated at the blind zone and far field, and Table III outlines the whole coverage performance. In the case of near-field design, if only the main cuts are observed, their evaluation in the far-field seems to be similar to the blind zone, with a slight degradation in ripple. However, if the entire angular range is evaluated, a significant drop in compliance can be seen, decreasing from 100% to 55.29%. Similarly, the ripple of the compliant points is noticeably higher (from 0.29 to 0.95), and the point that do not comply are on average 1.46 dB from the 1 dB requirement. The far-field case is much more critical, as when evaluating in the blind zone, the 1 dB specification is practically not met (7.95%). Additionally, the mean error is above 1.40 dB with a

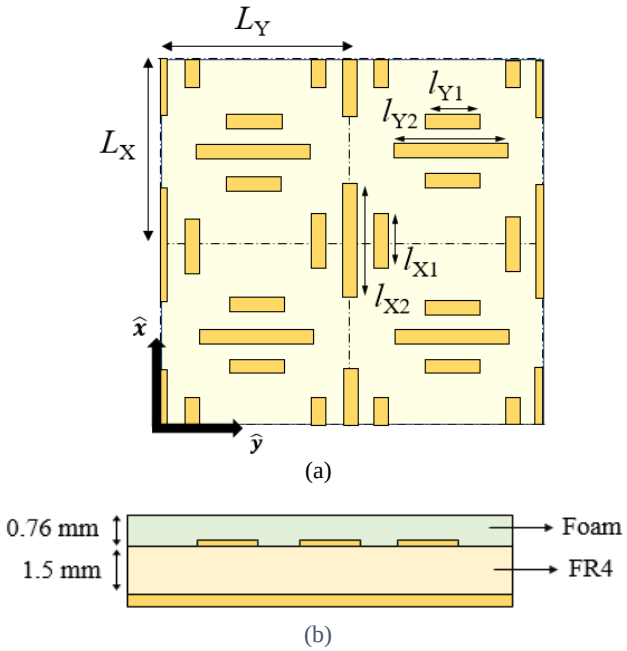

Fig. 9 (a) Upper view showing the reflectarray periodic structure and (b) lateral view showing the stack-up configuration.

mean ripple of 2.60 dB, which is quite far from specifications. Thus, designing SES by imposing conditions in the far field when the coverage is in the near field can lead to a strong degradation of the expected coverage.

C. *Design procedure*

The SES has been designed using dual-LP reflectarray cells, depicted in Fig. 9, which enable independent control of the phase response in each linear polarization (H- and V-pol) at 27.6 GHz. The SES periodicity is $L_X \times L_Y$. The phase shifts introduced in V-pol are controlled by groups of three rectangular dipoles that are oriented in the x-axis direction (the required phase shift can be achieved by adjusting the lengths l_{X1} and l_{X2} in each cell), while the phase shifts in H-pol are achieved using groups of three dipoles parallel to the y-axis (by adjusting the lengths l_{Y1} and l_{Y2} in each cell). In each group of three dipoles, the lateral ones have equal length, in order to reduce the levels of cross-polarization. The orthogonal sets of dipoles are arranged as shown in Fig. 9(a), with half-a-period shifting along x and y axes, in order to place both sets of dipoles on a single substrate layer. The SES stack-up consists of two dielectric layers, see Fig. 9(b). The lower substrate is FR4 (Isola FR408HR) with 1.5 mm thickness, $\epsilon_r = 3.628$ and $\tan\delta = 0.0098$. This substrate has the printed dipoles on its upper side, and it is backed by the ground plane. The upper substrate is a foam with 0.762 mm thickness, $\epsilon_r = 1.532$ and $\tan\delta = 0.012$, which protects the dipoles printed on the FR4.

The unit cells shown in Fig. 9 provide a smoother phase response and greater range of phase variation than other unit cells with a simpler pattern of printed elements (e.g., the rectangular patches used in [29]). Moreover, they provide a robust performance under large incidence angles, such as those of the indoor scenario depicted in Fig. 4. Note that SES cells based on stacked rectangular patches [45] can provide a similar performance, but they require several layers of printed elements

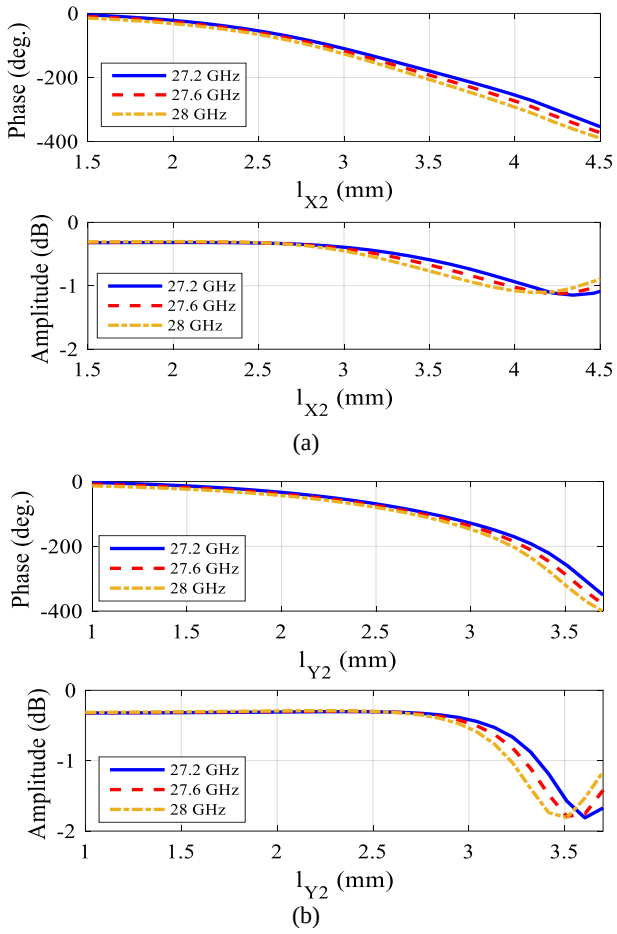

Fig. 10 Simulated phase and amplitude of the copolar reflection coeffcients at several frequencies under normal incidence: (a) V-polarization and (b) H-polarization

(which would result in larger weight, volume, and fabrication cost of the SES panel). The unit cells used in this work have a single metallization layer and enable an independent control of the phase response in each linear polarization, thanks to the uncoupling between the orthogonal sets of dipoles (as shown in [46]), which is not the case of other single-layer cells with twofold symmetry [47]-[48]. In this case, the beam requirements defined in Section IV.A are the same for both polarizations (to ensure the users' connectivity in the blind zone), but the same unit cells can be used to design an SES with different beam requirements in each polarization.

The geometric parameters of the SES cell have been optimized to provide a linear phase response of the reflection coefficients associated to the H- and V-pol at the operating frequencies of the SES. The unit cell dimensions are set to $L_X = 5$ mm and $L_Y = 4.1$ mm, both values smaller than $\frac{\lambda}{2}$ at the $27-28$ GHz band. The reason for choosing $L_Y < L_X$ (instead of $L_Y = L_X$) is to improve the performance of the cells under strong oblique incidence along the y-axis, which is a typical situation in many standard deployment scenarios [23], [27]. The width of the printed dipoles is fixed to 0.25 mm, and separation between adjacent parallel dipoles is 0.6 mm (from center to center). The lengths l_{X1} and l_{X2} are adjusted cell by cell to control the phase introduced in V-pol, while the lengths l_{Y1} and

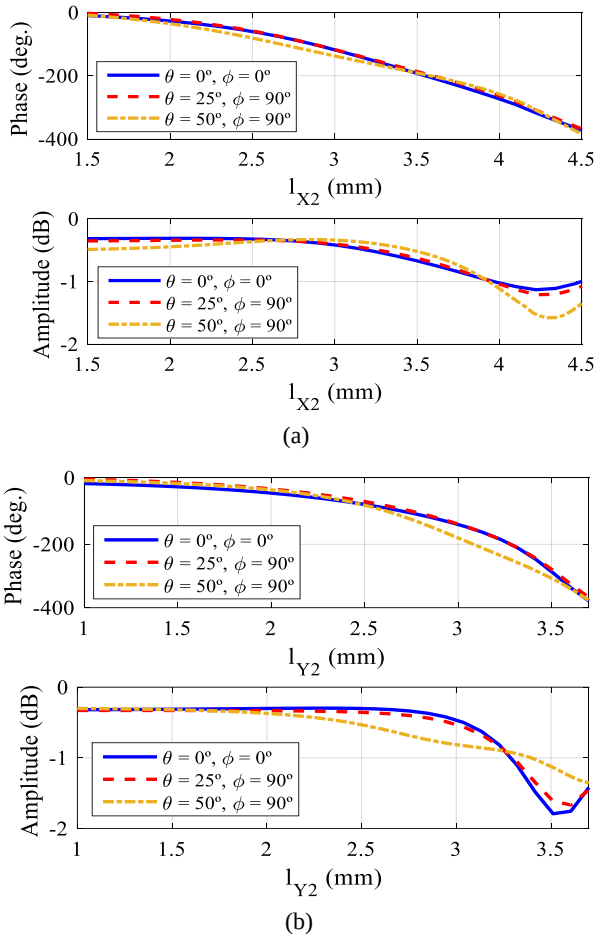

Fig. 11 Simulated phase and amplitude of the copolar reflection coeffcients at central frequency (27.6 GHz) under different incidence angles: (a) V-polarization and (b) H-polarization.

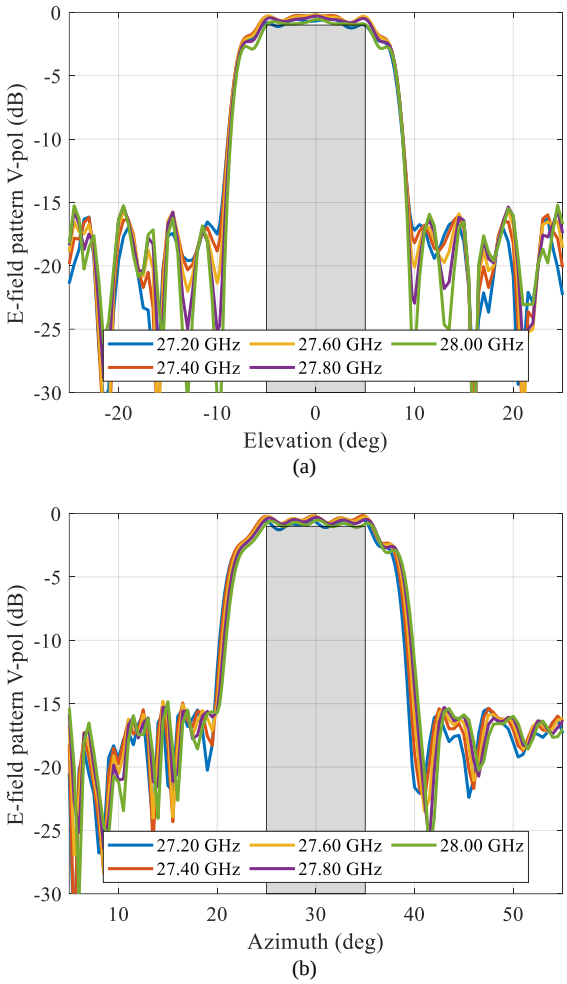

Fig. 12. Comparison of the near-field radiated by the design at 12 m (blind zone) through an analysis based on MoM and full wave simulations at different frequencies (V-pol). (a) Elevation (b) Azimuth cuts. The field is normalized to the maximum of the coverage.

l_{Y2} are used to implement the required phase shifts in H-pol. In order to have a single design variable for each linear polarization (l_{X2} and l_{Y2}), a fixed scale factor is considered between the lengths of the central and lateral dipoles in each group, so that $l_{X1} = 0.57\ l_{X2}$ and $l_{Y1} = 0.72\ l_{Y2}$.

The analysis of the unit cell has been performed by an in-house electromagnetic code based on the Method of Moments (MoM) and the local periodicity assumption [49], which is used to obtain the amplitude and phase of the reflection coefficients defined in (7). The results of the copolar reflection coefficients ρ_{xx} and ρ_{yy}, associated to V- and H-pol, at the central and extreme operating frequencies of the SES (27.2, 27.6, and 28 GHz) are depicted in Fig. 10(a) and Fig. 10(b) as a function of the central dipole length for each polarization (l_{X2} and l_{Y2}). The simulations in Fig. 10 have been carried out considering normal incidence. The reference plane for the phase computation is the top surface of the cell (upper face of the foam layer, which would correspond to the plane $z = 0$). Similar performance is achieved in both polarizations, whit a phase range of around 400° and a smooth phase variation.

The effect of the incidence angles in the copolar reflection coefficients ρ_{xx} and ρ_{yy} at the central frequency (27.6 GHz) is analyzed in Fig. 11. The incidence cases evaluated range from normal incidence to strong oblique incidence along the y-axis ($\theta = 50°, \varphi = 90°$), which is a typical characteristic in many standard deployment scenarios for SES [23], [27]. Note that the current SES design is associated to the intermediate incidence case ($\theta = 25°, \varphi = 90°$). As shown in Fig. 11, the cell exhibits a robust behavior under strong oblique incidence conditions, keeping more than 360° of phase variation and similar levels of reflection losses. To obtain the layout of the 40 cm × 40 cm SES panel, the length of the printed dipoles has been adjusted cell by cell according to the objective phase distributions achieved in Section IV.B by the NF synthesis. To simplify this process, the x-oriented and y-oriented dipoles are designed separately, thanks to the uncoupling between the two linear polarizations. Note that the real incidence angles from the feed on each SES unit cell are considered in this design process.

D. Smart Electromagnetic Skin Performance

The phase distribution resulting from the near-field synthesis has been used to design the SES. In the design process, the lengths of the central dipoles have been adjusted to introduce the required phase shift in both polarizations. The layout is evaluated through an analysis based on MoM assuming local periodicity, and a full-wave simulation using CST Microwave

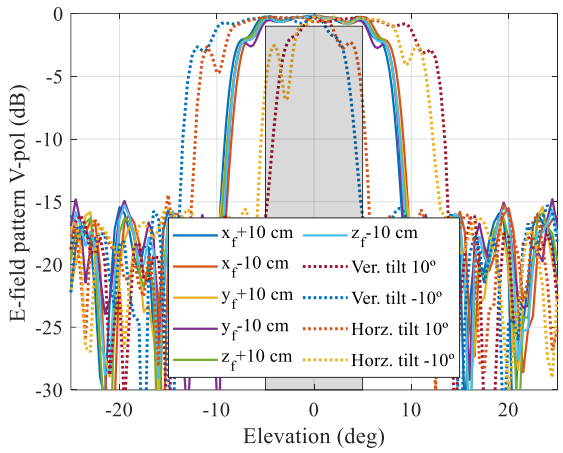

(a)

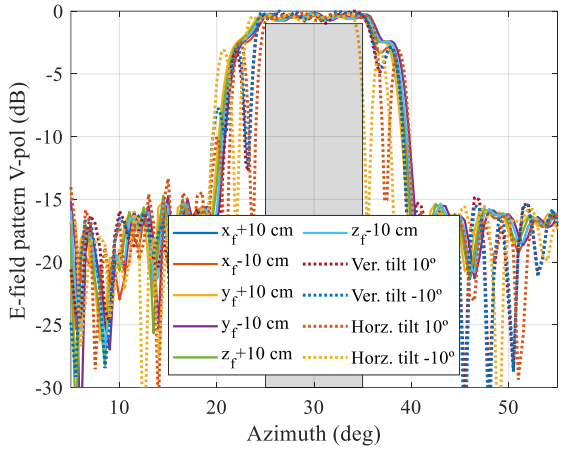

(b)

Fig. 13. Evaluation of the error in the position of the SES at the central frequency and V-pol, evaluated at the coverage area.

Table IV. Comparison of the compliance of the near-field design evaluated in the coverage at several frequencies.

Frequency (GHz)	Analysis	1 dB (%)	Mean Ripple*	Ripple coverage**	Mean error***
27.20	MoM	77.31	0.68	0.79	0.18
27.40	MoM	99.14	0.42	0.43	0.05
27.60	MoM	100	0.45	0.45	-
27.60	CST	87.30	0.21	0.49	0.49
27.80	MoM	97.69	0.56	0.57	0.06
28.00	MoM	70.76	0.74	0.82	0.15

*Mean ripple of the field within 1-dB compliance.
**Mean ripple within the angular range of the coverage.
***Mean error of the field outside the compliance and 1-dB ripple.

Studio. For the design, not only the coverage obtained at the center frequency (27.6 GHz) is evaluated, but also its behavior across the band for the 800 MHz associated with the two adjacent 5G channels is analyzed. Fig. 12 shows the main cuts of the near-field pattern at different frequencies within this bandwidth. The band response is very stable, achieving a ripple and angular margin very similar, as well as SLL, which always remains below −15 dB. Table IV summarizes the compliance percentage for the band. Excluding extreme frequencies, nearly perfect compliance with the 1 dB ripple is reached for the entire angular range. In the case of edge frequencies, the compliance decreases to 70%. However, the mean error of point outside specifications is barely 0.18 dB in the worst case (27.20 GHz).

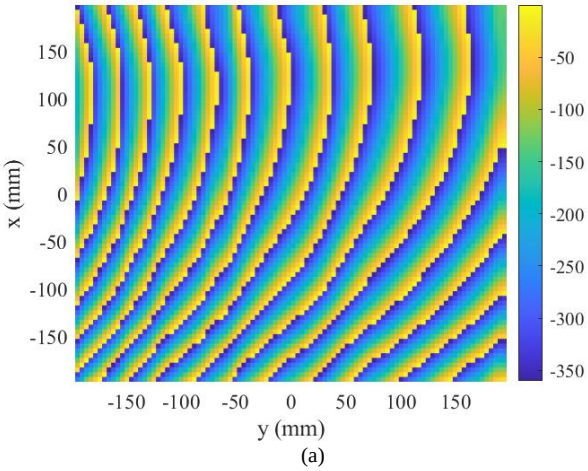

(a)

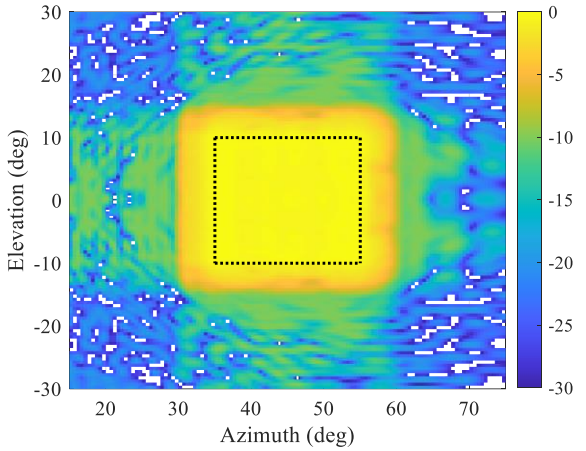

(b)

Fig. 14. (a) Phase-shift distribution on the SES surface after the Phase-Only Synthesis and (b) near-field pattern (dB) at 10 m obtained with this phase-shift distribution. The field is normalized to its maximum within the coverage, whose limits are shown in dotted black line.

Table V. Comparison of the compliance of the near-field design evaluated in the coverage considering errors in the location of the SES.

Position	Variation	1 dB (%)	Mean Ripple*	Ripple coverage**	Mean error***
x_f	+10 cm	99.34	0.44	0.44	0.19
	−10 cm	99.34	0.43	0.43	0.18
y_f	+10 cm	99.60	0.46	0.46	0.19
	−10 cm	99.67	0.44	0.44	0.22
z_f	+10 cm	100	0.45	0.57	0.06
	−10 cm	99.86	0.45	0.82	0.15
Vertical tilt	+10°	54.76	0.52	3.16	5.35
	−10	55.42	0.47	3.19	5.57
Horizontal tilt	+10	67.19	0.43	1.74	3.41
	−10	62.98	0.52	1.84	3.09

*Mean ripple of the field within 1-dB compliance.
**Mean ripple within the angular range of the coverage.
***Mean error of the field outside the compliance and 1-dB ripple.

The maximum ripple across the entire angular range is only 1.20 dB. Thus, the coverage obtained is very stable within these 800 MHz. Similarly, full-wave simulations show a high degree of agreement with MoM-based analysis. The decrease on the percentage is associated to the specular reflection of the BS, which is close to the coverage area and produce a distortion on the ripple. However, the results validate proposed analysis and design technique.

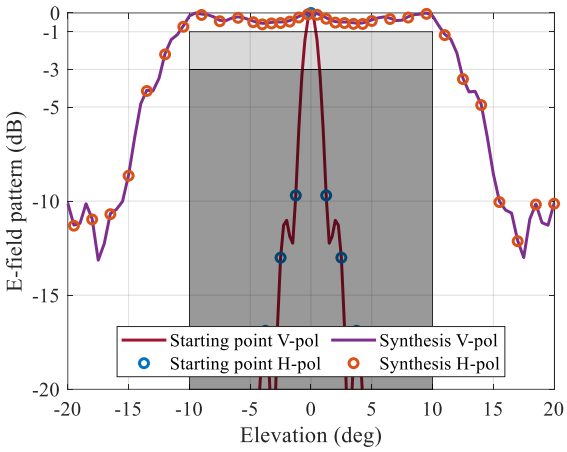

(a)

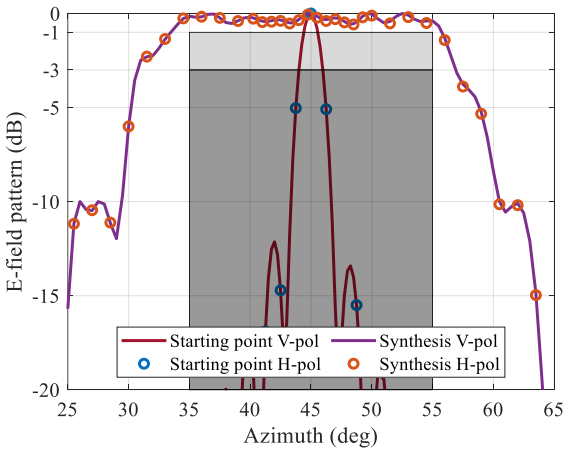

(b)

Fig. 15. Main cuts of the near-field pattern at 10 m in (a) elevation (azimuth = 45 deg) and (b) azimuth (elevation = 0 deg) for the starting and synthesis point for both linear orthogonal polarizations.

Given that the SES is located tens of meters away from the feeder (base station), and will be installed on a wall, the tolerance of the design to SES positioning errors has been analyzed. For this analysis, it has been considered that the SES is not installed in the design location, but rather variation of ± 10 cm are introduced in each direction. To do so, the response of the SES considering a displacement of the feeder position (x_f, y_f, z_f) has been analyzed. Fig. 13 shows the main coverage cuts for these cases, and Table V contains the compliance evaluation for all analyses. The design, for the analyzed cases, prove to be very robust, always maintaining compliance above 99%. Thus, significant errors in SES positioning should not affect the obtained performance. It should be noted that the BS is far enough away to consider that there is very uniform illumination on the surface, but also in neighboring areas.

Another complementary analysis that has been carried out is to consider a tilt of the SES with respect to its original position. A vertical tilt of $\pm 10°$ (with respect to the x-axis, see Fig. 4), and a horizontal tilt of $\pm 10°$ (with respect to y-axis, see Fig. 4) have been considered. The main cuts and compliance are outlined in Fig. 13 and Table V, respectively. In this case, compliance sharply declines. However, it is not that the ripple in the coverage area is increasing, but rather that by producing

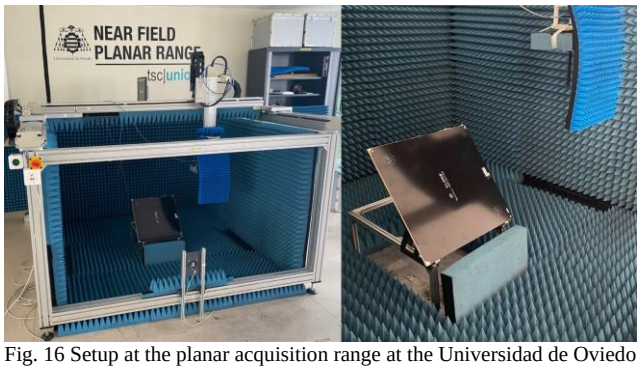

Fig. 16 Setup at the planar acquisition range at the Universidad de Oviedo to evaluate the coverage generated by the SES panel manufactured by Metawave Corp. in Ka-band.

the tilt, the reflected outgoing beam is also tilted to another direction, as seen in Fig. 13(a). Hence, this type of errors is much more critical than other, as it deflects the beam in a different direction than the expected one.

V. Experimental Validation of a Smart Electromagnetic Skin for Indoor Scenarios

A. Design of the Smart Electromagnetic Skin

For practical reasons related to the experimental validation, it is not feasible to use a BS as a feeder. Therefore, a new design is carried out considering a feeder close to the SES, at a distance of 80 cm, in order to perform an experimental validation. Using the same panel size, and unit cell, the feeder is now located at $(x, y, z) = (0, -0.566, 0.566)$ m. At this distance, the $\frac{F}{D}$ ratio is approximately 2, ensuring that the SES is in the far field of the feeder and there is no effect of spatial diversity of the unit cell. The central operating frequency of the SES is 27.6 GHz with a bandwidth of 800 MHz to cover two 5G channels of 400 MHz each.

Using the scenario depicted in Fig. 4, the electric requirements are changed to show another case where SES can be useful. To proper cover the new blind zone, the reflected beam in dual-LP must point at $\psi_{az} = 45°$ in azimuth and $\psi_{el} = 0°$ in elevation. The input angles from the feed are $-45°$ in azimuth and 0° in elevation, so the reflected beam is produced at the specular direction. The half-power beamwidth must be $\text{HPBW}_{\text{az}} = 20°$ and $\text{HPBW}_{\text{el}} = 20°$ in azimuth and elevation at a distance of 10 m, respectively. Note that the set up angular range is quite challenging. Similar to the previous case, a pencil beam would provide 2° in both directions. Due to the significant increase in the angular margin, the accepted ripple requirement is relaxed to allow for 3 dB ripple.

The design of the SES is again conducted using a near-field pattern synthesis, which is based on the Intersection Approach and the previous techniques described (enhanced functional, multi-stage, and DFCs) to improve the converge and successfully reach the desired result. Starting from the phase-shift distribution obtained through (12), two POS processes are carried out, one for each linear polarization. In this case, the whole process for the V-pol took 14 stages, while 12 stages were needed for the H-pol. The output of the syntheses is the phase-shift distribution of the SES that radiates the near-field pattern that satisfies the coverage specifications. Fig. 14(a)

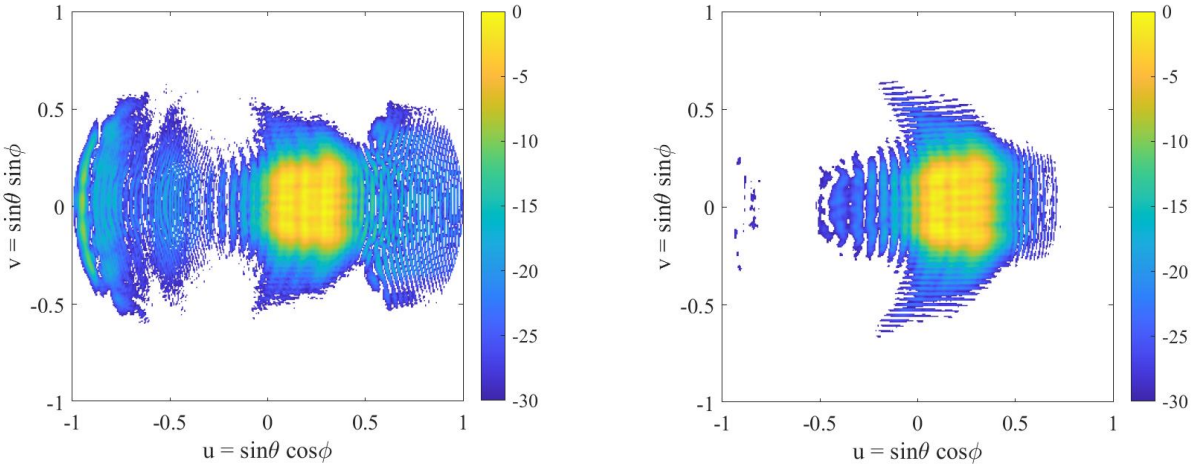

Fig. 17 Measured Near field pattern (dB) obtained after the NF-NF transformation in uv-coordinated at 27.7 GHz for both (a) V- and (b) H- pol at 10 m.

shows the output for the V-pol, while Fig. 14(b) shows the near-field pattern at 10 m radiated by the solution. The high outgoing angles produce a fast variation of the phase-shift distribution along the surface of the SES. Fig. 15 compares the coverage main cuts in elevation and azimuth for the starting point and the synthesized pattern for both polarizations at a distance of 10 m. A major improvement is reached in both directions, successfully covering the entire angular margin. The pencil has been broadened more than 16°, with a ripple lower than 3 dB, and an average ripple of 1 dB. Thus, the specifications are met for both polarizations, reaching slightly better results for the V-pol.

Observing Fig. 14(b) and Fig. 15, the results show that the field pattern accomplished the tight requirements, broadening the pencil beam and reaching a uniform power density within the 20° by 20° angular range. Moreover, out of the coverage the field is notably low with a field decay about 30 dB with respect to the average level of the coverage, avoiding the radiation in undesired directions, and 15 dB in the main cuts. The starting coverages obtained with the pencil beam meet a 2.36% and 2.44% of the requirements for the V- and H-pol, respectively. After the synthesis processes, the compliance increases up to 100% and 89.79% for the V- and H-pol, respectively. It is worth noting the high complexity of those syntheses due to the tight requirements needed. The pencil beam in azimuth and elevation is broaden over 20° starting from 2°. Furthermore, the starting point within this angular margin generates several nulls (see Fig. 15) that must be filled to reach the uniform power density.

The SES is designed using the dual-LP unit cell shown in Fig. 9, which allows for independent control of the phase response in each linear polarization. The design of the elements and unit cell performance are the ones described in Section IV. Overall, the length of the dipoles l_{X1} and l_{Y1} are adjusted to produce the desired phase shift.

B. Measurement setup

The designed SES panel has been manufactured and measured to evaluate the performance of the coverage. The measurements have been carried out in the planar acquisition range at the Universidad de Oviedo. The dimensions of the system are $1.5 \times 1.5 \times 1.5$ m^3. Therefore, it is not feasible to directly measure the near field pattern at the coverage. The measurement is divided into two steps: the field is first measured at a plane close to the aperture of the SES, about 500 mm from the center of the panel; second, the coverage is obtained through a NF-NF transformation using GRASP from TICRA [50]. The field is got in a grid of 800×800 (mm^2) to ensure that more than 98% of the radiated power is captured and the NF-NF transformation is properly carried out.

Fig. 16 presents the setup used in the planar acquisition range. The illumination of the base station is emulated by a horn antenna of 15 dBi gain placed at 800 mm from the center of the panel. The horn antenna provides a uniform field distribution on the panel, similar to the one expected from the base station. Then, the reflected field is captured in a plane parallel to the aperture of the probe, which is an open-ended WR28 waveguide. The measurements are carried out at several frequencies from 26 to 30 GHz, which cover more bandwidth than designing requirements.

From now on, the copolar component of the near field is defined as the main component of the field associated with the copolar radiation of the feeder, while the cross-polar is the orthogonal component considering linear polarization.

C. Measurements: Near-field coverage

The copolar of the near field reradiated by the SES at the central frequency (27.6 GHz) at the users' distance (10 m) for both linear polarizations is shown in Fig. 17 (in uv-representation). The pattern exhibits a uniform field distribution within the angular range of the blind area in dual linear polarization. In the case of the V-pol, there is a diffraction pattern associated with the planar acquisition range. A better comparison with the POS' results can be obtained from Fig. 18, which shows the main cut in azimuth at several frequencies.

The main cuts of the two orthogonal polarizations exhibit an almost uniform field distribution. The V-pol exhibits a quite flat response, nearly achieving the required ripple within the desired angular range, as it was expected from the results of the pattern synthesis. At the design frequency (27.6 GHz), the

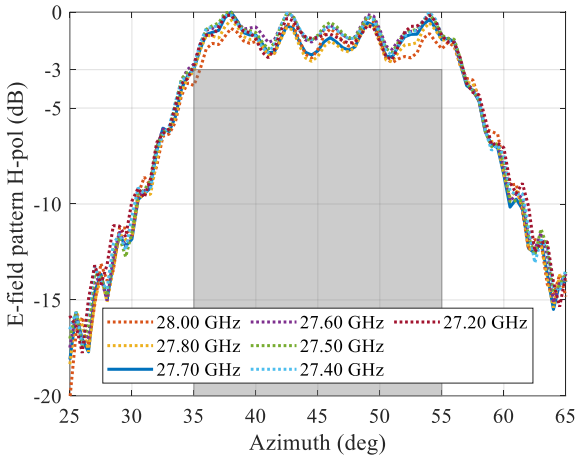

(a)

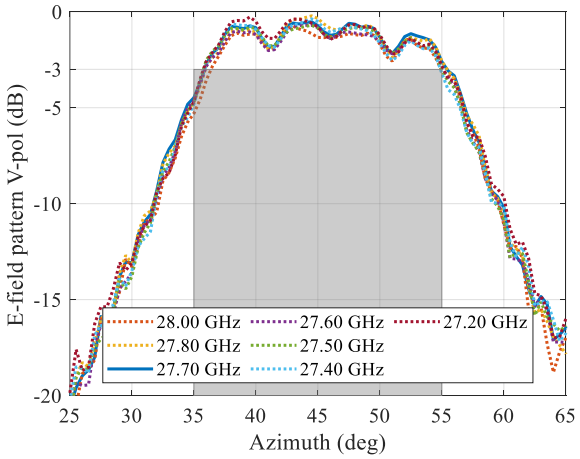

(b)

Fig. 18. Main cuts in azimuth (elevation = 0 deg) for the measured near field at several frequencies for (a) H-pol and (b) V-pol. The field is normalized to the maximum of the coverage.

measurements clearly satisfy the 3 dB ripple specification. A similar response is obtained within the bandwidth analyzed. In the case of the H-pol the measurements are slightly better, and the near-field distribution presents less than 3 dB ripple within the 20° range. The response at the design frequency is kept within the 800 MHz bandwidth.

The overall in-band response of the SES is stable within the 800 MHz, from 27.2 to 28 GHz. The amplitude slightly increases its ripple in some frequencies; however, the 3 dB specification is still satisfied in all the cases. From Fig. 17 it can be derived that the diffraction may have an impact on the measurements, just by increasing the ripple. In the case of the *H*-pol the 3 dB ripple is always fulfilled, having a mean ripple from 1.59 dB (28 GHz) to 0.90 dB (27.60 GHz). At the design frequency (27.70 GHz) the mean ripple is 1.32 dB. For the *V*-pol the ripple slightly increases but the compliance is always over a 97%. Only at 28 GHz it decreases down to nearly 95%. In terms of the mean ripple, it goes from 1.65 dB (28 GHz) to 1.21 dB (27.40 GHz), while at 27.70 GHz the mean value is 1.26 dB.

VI. Conclusions

This work addresses the design of a passive Reflective Intelligent Surface (RIS), also known as Smart Electromagnetic Skin (SES), for improving coverage in mm-Wave indoor scenarios. The design is based on the assumption that users will be in the near field of the RIS, and as the primary innovation, the coverage generated will not be a focused spot but rather on an adapted shaped beam tailored to the desired blind zone coverage. To achieves this, a design technique is introduced that allows for the control of the near field radiated by the RIS. In this way, a Phase-Only Synthesis is employed to obtain a phase-shift distribution that generates the desired shaped beam.

The synthesis technique includes figure of merits within the cost function that are directly related to the radiation parameters, such as the desired ripple within the coverage or the maximum field level or SLL outside it. This modification in the cost function enhances the convergence of the synthesis as it seeks a highly complex pattern. Initially, a pencil beam in the near field is used, generating a coverage within an angular margin of approximately $2° \times 2°$ (considering a ripple of 3 dB). After the synthesis, the obtained phase-shift distribution results in an angular coverage of $20° \times 20°$ (for the 3 dB ripple requirement).

These results are employed to design a passive RIS using a unit cell based on coplanar dipoles, allowing control of two orthogonal linear polarizations. A prototype is fabricated and measured in a planar acquisition range. Then, a near field to near field transformation is applied to finally obtained the near-field pattern at the coverage. The measurements align with the obtained results, generating a highly uniform field distribution that would cover a 20° by 20° blind zone in the mm-Wave band. Notably, this behavior remains consistent over an 800 MHz bandwidth, enabling coverage of a standard 5G channel. Both the presented technique and the obtained results demonstrate that the use of passive RIS is a valuable element in enhancing 5G coverage, particularly in indoor scenarios where blind zones are particularly critical. Furthermore, such scenarios require the use of suitable analysis and near-field-based techniques, enabling not only near-field focused approaches but also shaped near-field patterns like those used in far-field communications.

Appendix

Near Field using Fresnel Formulation

The near field of a focused aperture can be analytically derived from the Fresnel equation (3). Considering the analytical tangential field described in (9), the near field is now expressed as

$$\boldsymbol{E}(\boldsymbol{r}) = \frac{j}{2\lambda}\frac{e^{-jkz}}{R}\int_S E_0 e^{jk_0\frac{(x^2+y^2)}{2F}} e^{-jk\left(\frac{(x-x')^2+(y-y')^2}{2z}\right)}(\cos\theta + \boldsymbol{u}_z\cdot\boldsymbol{s})dxdy \qquad (14)$$

Assuming that the calculation region of the field is confined to small angles from the z axis, $\cos\theta \approx 1$ and $\boldsymbol{u}_z \cdot \boldsymbol{s} \approx 1$. Thus, expanding the quadratic phase terms with the phase of the tangential field and factoring, (NN) might be written as

$$\boldsymbol{E}(\boldsymbol{r}) = \frac{jE_0}{\lambda}\frac{e^{-j\xi}}{R}\int_S e^{-\frac{jk(F-z)}{2z\,F}\left[\left(x-\frac{F}{F-z}x'\right)^2+\left(y-\frac{F}{F-z}y'\right)^2\right]}dxdy \qquad (15)$$

where $\xi = k\left[z - \frac{\frac{F}{F-z}-1}{2z}(x'^2 + y'^2)\right]$. If we now rewrite $\frac{F}{F-z}$ as ψ, and expand the exponential of the integrand using trigonometric identities, the field is expressed as

$$\begin{aligned}\boldsymbol{E}(\boldsymbol{r}) = \frac{jE_0}{\lambda}\frac{e^{-j\xi}}{R}\iint_S \Big[\cos\frac{k}{2\psi z}(x-\psi x')^2 \\ - j\sin\frac{k}{2\psi z}(x-\psi x')^2\Big]\Big[\cos\frac{k}{2\psi z}(y \\ - \psi y')^2 - j\sin\frac{k}{2\psi z}(y-\psi y')^2\Big]dxdy\end{aligned} \tag{16}$$

Applying the Fubini's Theorem in (16), considering that the SES aperture ($D_x \times D_y$, see Figure 1) is the integration domain S, and defining the Fresnel integrals as

$$C(n) = \int_0^n \cos\frac{\pi}{2}t^2 dt \tag{17}$$

$$S(n) = \int_0^n \sin\frac{\pi}{2}t^2 dt \tag{18}$$

(16) might be now expressed in terms of these integrals as

$$\begin{aligned}\boldsymbol{E}(\boldsymbol{r}) = jE_0\frac{z\psi}{2}\frac{e^{-j\xi}}{R}\Bigg[C\left(\frac{D_x+2\psi x'}{\sqrt{2z\psi\lambda}}\right)+C\left(\frac{D_x-2\psi x'}{\sqrt{2z\psi\lambda}}\right) \\ - jS\left(\frac{D_x+2\psi x'}{\sqrt{2z\psi\lambda}}\right)-jS\left(\frac{D_x-2\psi x'}{\sqrt{2z\psi\lambda}}\right)\Bigg] \\ \cdot\Bigg[C\left(\frac{D_y+2\psi x'}{\sqrt{2z\psi\lambda}}\right)+C\left(\frac{D_y-2\psi x'}{\sqrt{2z\psi\lambda}}\right) \\ - jS\left(\frac{D_y+2\psi x'}{\sqrt{2z\psi\lambda}}\right)-jS\left(\frac{D_y+2\psi x'}{\sqrt{2z\psi\lambda}}\right)\Bigg]\end{aligned} \tag{19}$$

The computation of $C(n)$ and $S(n)$ require the use of numerical methods, tables or the use of the Cornu spiral.

NEAR FIELD USING PRINCIPLE OF SUPERPOSITION

From (8), only the contribution of each subdomain needs to be computed. $\boldsymbol{E}_{SD,i}$ is the far-field contribution of the i-th subdomain, which is considered as a small radiating aperture. To do this, we start from the electric and magnetic potential vectors, which are defined for a single subdomain as

$$\boldsymbol{A}^{SD}(\boldsymbol{r}) = \frac{\mu}{4\pi r}e^{-jkr}\iint_{SD}\boldsymbol{J}^{SD}(r')e^{jk\hat{\boldsymbol{r}}\cdot\boldsymbol{r}'}dS \tag{20}$$

$$\boldsymbol{F}^{SD}(\boldsymbol{r}) = \frac{\epsilon}{4\pi r}e^{-jkr}\iint_{SD}\boldsymbol{M}^{SD}(r')e^{jk\hat{\boldsymbol{r}}\cdot\boldsymbol{r}'}dS \tag{21}$$

where $\boldsymbol{J}^{SD}$ and $\boldsymbol{M}^{SD}$ are the electric and magnetic superficial currents on the subdomain.

Now, from (20), (21), the radiated electric field can be expresses as a function of the spherical components of both potential vectors.

$$\begin{aligned}\boldsymbol{E}^{SD} = j\omega\big(\hat{\boldsymbol{r}}\times(\hat{\boldsymbol{r}}\times\boldsymbol{A}^{SD})\big)+j\omega\eta(\hat{\boldsymbol{r}}\times\boldsymbol{F}^{SD}) \\ = -j\omega\Big(\big(A_\theta^{SD}+\eta F_\varphi^{SD}\big)\hat{\boldsymbol{\theta}} \\ + \big(A_\theta^{SD}-\eta F_\varphi^{SD}\big)\hat{\boldsymbol{\varphi}}\Big)\end{aligned} \tag{22}$$

For a planar aperture contained within a perfect electrical conductor (PEC) in the XY plane (similar to the aperture of Fig. 1), the electric and magnetic currents can be related to the magnetic and tangential field through [36]

$$\boldsymbol{J}^{SD} = \hat{\boldsymbol{n}}\times\boldsymbol{H}^{SD} \tag{23}$$

$$\boldsymbol{M}^{SD} = \hat{\boldsymbol{n}}\times\boldsymbol{E}^{SD} \tag{24}$$

where $\hat{\boldsymbol{n}}$ is $\hat{\boldsymbol{z}}$ in this case, and $\boldsymbol{H}_{SD}$ and $\boldsymbol{E}_{SD}$ are the magnetic and electric tangential field, respectively.

Applying (23) and (24) to (20) and (21), the potential vectors can be now expressed in terms of the tangential field as

$$\boldsymbol{A}^{SD}(\boldsymbol{r}) = \frac{\mu}{4\pi r}e^{-jkr}\hat{\boldsymbol{z}}\times\iint_S\boldsymbol{H}^{SD}(r')e^{jk\hat{\boldsymbol{r}}\cdot\boldsymbol{r}'}dS \tag{25}$$

$$\boldsymbol{F}^{SD}(\boldsymbol{r}) = -\frac{\epsilon}{4\pi r}e^{-jkr}\hat{\boldsymbol{z}}\times\iint_S\boldsymbol{E}^{SD}(r')e^{jk\hat{\boldsymbol{r}}\cdot\boldsymbol{r}'}dS \tag{26}$$

where the integrals define the well-known Spectral Functions ($\boldsymbol{P}$ and $\boldsymbol{Q}$). If we defined $\hat{\boldsymbol{r}}\cdot\boldsymbol{r}' = ux'+vy'$, being $u = \sin\theta\cos\phi$; $v = \sin\theta\sin\phi$; $\boldsymbol{r}' = x'\cdot\hat{\boldsymbol{x}}+y'\cdot\hat{\boldsymbol{y}}$; and $\hat{\boldsymbol{r}} = \hat{\boldsymbol{x}}\sin\theta\cos\varphi+\hat{\boldsymbol{y}}\sin\theta\cos\phi+\hat{\boldsymbol{z}}\cos\theta$, the Spectral Functions can be now written as following

$$P_{x,y}(u,v) = \iint_S E_{x,y}^{SD}(x',y')e^{jk(ux'+vy')}dx'dy' \tag{27}$$

$$Q_{x,y}(u,v) = \iint_S H_{ax}^{SD}(x',y')e^{jk(ux'+vy')}dx'dy' \tag{28}$$

Now, (22) can be expanded to calculate its spherical components in terms of $\boldsymbol{P}$ and $\boldsymbol{Q}$ as

$$\begin{aligned}E_\theta^{SD} = \frac{jk}{4\pi r}e^{-jkr}\big(P_x\cos\varphi+P_y\sin\varphi \\ -\eta\cos\theta\big(Q_x\sin\varphi-Q_y\cos\varphi\big)\big)\end{aligned} \tag{29}$$

$$\begin{aligned}E_\varphi^{SD} = -\frac{jk}{4\pi r}e^{-jkr}\big(\cos\theta\big(P_x\sin\varphi-P_y\cos\varphi\big) \\ +\eta\big(Q_x\cos\varphi+Q_y\sin\varphi\big)\big)\end{aligned} \tag{30}$$

These expressions refer to the First Principle of Equivalence [36]. However, since the subdomain SD is considered as a small aperture (SD is lower than $0.5\lambda\times0.5\lambda$) on a ground plane, it is possible to employ the Second Principle of Equivalence [36]. In this case, it is only necessary to calculate the magnetic potential vector to obtain the radiated electric field, allowing us to rewrite (29) and (30) solely in terms of the Spectrum Function $\boldsymbol{P}$ as

$$E_\theta = \frac{jk}{2\pi r}e^{-jkr}\big(P_x\cos\varphi+P_y\sin\varphi\big) \tag{31}$$

$$E_\varphi = -\frac{jk}{2\pi r}e^{-jkr}\big(\cos\theta\big(P_x\sin\varphi-P_y\cos\varphi\big)\big) \tag{32}$$

It is worth noting that these expressions are the same as those obtained using the stationary-phase approximation [51] and evaluating the integrals asymptotically. Similarly, if we apply the stationary-phase assumption (this means assuming that the tangential field on the subdomain is constant) to (27), the calculation of $\boldsymbol{P}$ for a subdomain of dimensions p_x and p_y would be

$$\begin{aligned}P_{x/y} = E_0e^{j\phi_0}\iint_{SD}e^{jk(x\sin\theta\cos\varphi+y\sin\theta\sin\varphi)}dxdy \\ = E_0e^{jk_0\frac{(x^2+y^2)}{2F}}p_xp_y\Big[\operatorname{sinc}\Big(\frac{k_0x\sin\theta\cos\varphi}{2}\Big) \\ \cdot\operatorname{sinc}\Big(\frac{k_0y\sin\theta\sin\varphi}{2}\Big)\Big]\end{aligned} \tag{33}$$

REFERENCES

[1] S. A. Busari et al., "5G millimeter-wave mobile broadband: Performance and challenges", IEEE Commun. Mag., vol. 56, no. 6, pp. 137-143, Jun. 2018.

[2] W. Hong et al., "The role of millimeter-wave technologies in 5G/6G wireless communications," IEEE Journal of Microwaves, vol. 1, no. 1, pp. 101-102, 2021.

[3] T. S. Rappaport et al., "Overview of millimeter wave communications for fifth-generation (5G) wireless networks–With a focus on propagation models", IEEE Trans. Antennas Propag., vol. 65, no. 12, pp. 6213–6230, Dec. 2017.

[4] M. Shafi *et al*., "Microwave vs. millimeter-wave propagation channels: Key differences and impact on 5G cellular systems", IEEE Commun. Mag., vol. 56, no. 12, pp. 14-20, Dec. 2018.
[5] S. Salous *et al*., "Millimeter-wave propagation: Characterization and modeling toward fifth-generation systems", IEEE Antennas Prop. Mag., vol. 58, no.6, pp. 115-127, Dec. 2016.
[6] K. Zheng, et al., "Performance and Measurement Analysis of a Commercial 5G Millimeter-Wave Network," IEEE Access, vol. 8, pp. 163996-164011, 2020.
[7] Q. Wu and R. Zhang, "Towards smart and reconfigurable environment: Intelligent Reflecting Surface aided wireless network", IEEE Commun. Mag., vol. 58, no. 1, pp. 106-112, Jan. 2020.
[8] P. Wang et al., "Intelligent Reflecting Surface-assisted millimeter wave communications: Joint active and passive precoding design," IEEE Trans. Veh. Technol., vol. 69, no. 12, pp. 14960-14973, Dec. 2020.
[9] S. Maci, "Reflective Intelligent Surfaces and metasurface antennas," 2023 IEEE Radio and Antenna Days of the Indian Ocean (RADIO), Balaclava, Mauritius, 2023, pp. 1-1.
[10] G. Oliveri et al., "Holographic Smart EM Skins for Advanced Beam Power Shaping in Next Generation Wireless Environments," in *IEEE Journal on Multiscale and Multiphysics Computational Techniques*, vol. 6, pp. 171-182, 2021.
[11] METAWAVE: Klone & Turbo (5G Connectivity). Accessed: Sep. 15, 2023. [Online]. Available: https://www.metawave.com/kloneturbo
[12] C. Huang et al., "Reconfigurable Intelligent Surfaces for energy efficiency in wireless communication", *IEEE Trans. Wireless Commun.*, vol. 18, no. 8, pp. 4157-4170, Aug. 2019.
[13] M. Nemati et al., "RIS-assisted coverage enhancement in millimeter-wave cellular networks", *IEEE Access*, vol. 8, pp. 188171-188185, 2020.
[14] Q. Wu and R. Zhang, "Intelligent Reflecting surface enhanced wireless network via joint active and passive beamforming", *IEEE Trans. Wireless Commun.*, vol. 18, no. 11, pp. 5394-5409, Nov. 2019.
[15] C. You et al., "Fast beam training for IRS-assisted multiuser communications", *IEEE Wireless Communications Letters*, vol. 9, no. 11, pp. 1845-1849, Nov. 2020.
[16] A. Bagheri et al., "Mathematical Model and Real-World Demonstration of Multi-Beam and Wide-Beam Reconfigurable Intelligent Surface," in IEEE Access, vol. 11, pp. 19613-19621, 2023.
[17] M. Barbuto et al., "Composite Vortex Manipulation as a Design Tool for Reflective Intelligent Surfaces," in *IEEE Antennas and Wireless Propagation Letters*, vol. 22, no. 10, pp. 2392-2396, Oct. 2023.
[18] J. Huang and J. A. Encinar, *Reflectarray Antennas*, IEEE Press/Wiley, Piscataway, New York, 2008.
[19] P. Mei et al., "A low-cost, high-efficiency and full-metal reflectarray antenna with mechanically 2-D beam-steerable capabilities for 5G applications", IEEE Trans. Antennas Propag., vol. 68, no. 10, pp. 6997-7006, Oct. 2020.
[20] Z.-Y. Yu et al., "A wide-angle coverage and low scan loss beam steering circularly polarized folded reflectarray antenna for millimeter-wave applications", IEEE Trans. Antennas Propag., vol. 70, no. 4, pp. 2656-2667, Apr. 2022.
[21] S. Costanzo et al., "Dual-band dual-linear polarization reflectarray for mmWaves/5G applications", IEEE Access, vol. 8, pp. 78183-78192, 2020.
[22] L. Zhang *et al*., "A single-layer 10–30 GHz reflectarray antenna for the Internet of Vehicles", IEEE Trans. Veh. Technol., vol. 71, no. 2, pp. 1480-1490, Feb. 2022.
[23] E. Martinez-de-Rioja et al., "Passive dual-polarized shaped-beam reflectarrays to improve coverage in millimeter-wave 5G networks," *15th Eur. Conf. Antennas Propag. (EuCAP)*, Dusseldorf, Germany, Apr. 2021.
[24] E. Martinez-de-Rioja et al., "Enhancement of 5G millimeter-wave coverage in indoor scenarios by passive shaped-beam reflectarry panels", *16th Eur. Conf. Antennas Propag. (EuCAP)*, Madrid, Spain, Mar. 2022.
[25] D. R. Prado et al., "Improved reflectarray phase-only synthesis using the generalized intersection approach with dielectric frame and first principle of equivalence", Int. Journal of Antennas and Propagation, vol. 2017, pp. 1-11, 2017.
[26] J. A. Zornoza and J. A. Encinar, "Efficient phase-only synthesis of contoured-beam patterns for very large reflectarrays," Int. J. RF Microw. C. E., vol. 14, no. 5, pp. 415–423, 2004.
[27] D. Martinez-de-Rioja et al., " A simple beamforming technique for intelligent reflecting surfaces in 5G scenarios", *2022 Int. Wor. Antenna Technology (iWAT)*, Dublin, Ireland, May 2022.
[28] Z. Lu et al., "Broadband reflectarray for milimeter wave coverage enhancement in indoor NLOS scenario", 2019 Cross Strait Quad-Reg. Rad. Sci. & Wirel. Techn. Conf., China, Jul. 2019.
[29] D. Kitayama et al., "5G radio access experiments on coverage expansion using metasurface reflector at 28 GHz," 2019 IEEE Asia-Pacific Microw. Conf. (APMC), Singapore, Dec. 2019.
[30] ''3GPP release 16 description,'' 3GPP, Tech. Rep. 3GPP TR 21.916 v16.0.0, 2020. [Online]. Available: https://www.3gpp.org/release-16.
[31] Á. F. Vaquero et al., "Demonstration of a reflectarray with near-field amplitude and phase constraints as compact antenna test range probe for 5G New Radio devices", IEEE Trans. Antennas Propag., vol. 69, no. 5, pp. 2715-2726, May 2021.
[32] J. Sherman, "Properties of focused apertures in the Fresnel region," *IRE Transactions on Antennas and Propagation*, vol. 10, no. 4, pp. 399-408, Jul. 1962.
[33] R. S. Elliot, *Antenna Theory and Design, Revised ED*, NJ, USA: John Wiley & Sons, 2003.
[34] Ming-Kuei Hu, "Some new methods of analysis and synthesis of near-zone fields," 1958 IRE International Convention Record, New York, NY, USA, 1960, pp. 13-23.
[35] G. Oliveri, M. Salucci and A. Massa, "Generalized Analysis and Unified Design of EM Skins," in IEEE Transactions on Antennas and Propagation, vol. 71, no. 8, pp. 6579-6592, Aug. 2023, doi: 10.1109/TAP.2023.3281073.
[36] W. L. Stutzman and G.A. Thiele, "Antenna Theory and Design," John Wiley & Sons. 1981.
[37] Système, Dassault. (2021). *CST Microwave Studio*. Accessed: Feb. 26, 2024. [Online]. Available: http://www.cst.com
[38] O. M. Bucci, G. Franceschetti, G. Mazzarella, and G. Panariello, "Intersection approach to array synthesis," *IEEE Proc.-H, Microw. Antennas Propag.*, vol. 137, no. 6, pp. 349-357, Dec. 1990.
[39] O. M. Bucci, G. D'Elia, G. Mazzarella, and G. Panariello, "Antenna pattern synthesis: a new general approach," *Proc. IEEE*, vol. 82, no. 3, pp. 358-371, Mar. 1994.
[40] S. Loredo, G. León, and E. G. Plaza, "A fast approach to near-field synthesis of transmitarrays," *IEEE Antennas Wireless Propag. Lett.*, vol. 20, no. 5, pp. 648-652, May. 2021.
[41] Á. F. Vaquero, M. R. Pino and M. Arrebola, "Adaptive Field-to-Mask procedure for the synthesis of metalens antennas with complex near-field coverage patterns in 5G scenarios," *IEEE Transactions on Antennas and Propagation*, vol. 71, no. 9, pp. 7158-7171, Sept. 2023.
[42] A. Massa and M. Salucci, "On the design of complex EM devices and systems through the System-by-Design paradigm: A framework for dealing with the computational complexity," in *IEEE Transactions on Antennas and Propagation*, vol. 70, no. 2, pp. 1328-1343, Feb. 2022.
[43] D. R. Prado, M. Arrebola, M. R. Pino and G. Goussetis, "Contoured-Beam Dual-Band Dual-Linear Polarized Reflectarray Design Using a Multiobjective Multistage Optimization," in *IEEE Transactions on Antennas and Propagation*, vol. 68, no. 11, pp. 7682-7687, Nov. 2020.
[44] D. R. Prado, Á. F. Vaquero, M. Arrebola, M. R. Pino and F. Las-Heras, "Acceleration of Gradient-Based Algorithms for Array Antenna Synthesis With Far-Field or Near-Field Constraints," in IEEE Transactions on Antennas and Propagation, vol. 66, no. 10, pp. 5239-5248, Oct. 2018.
[45] R. Florencio, R. R. Boix, V. Losada, J. A. Encinar, E. Carrasco, and M. Arrebola, "Comparative study of reflectarrays based on cells with three coplanar dipoles and reflectarrays based on cells with three stacked patches", 6th Eur. Conf. Antennas Propag. (EuCAP), Prague, Czech Republic, 2012, pp. 3707-3710.
[46] R. Florencio, J. A. Encinar, R. R. Boix, V. Losada, and G. Toso, "Reflectarray antennas for dual polarization and broadband Telecom satellite applications," IEEE Trans. Antennas Propagat., vol. 63, no. 4, pp. 1234-1246, Apr. 2015.
[47] M. R. Chaharmir, J. Shaker, and H. Legay, "Broadband design of a single layer large reflectarray using multi cross loop elements", IEEE Trans. Antennas Propag., vol. 57, no.8, pp. 3363-3366, Aug. 2009.
[48] H. Hasani, C. Peixeiro, A. Skrivervik, and J. Perruisseau-Carrier, "Single-layer quad-band printed reflectarray antenna with dual linear polarization", IEEE Trans. Antennas Propag., vol. 63, no. 9, pp. 5522-5528, Sept. 2015.
[49] R. Florencio, R. R. Boix, E. Carrasco, J. A. Encinar, and V. Losada, "Efficient numerical tool for the analysis and design of reflectarrays based on cells with three parallel dipoles", Microw. Opt. Technol. Lett., vol. 55, no. 6, pp. 1212–1216, June 2013.
[50] TICRA: GRASP | Reflector Antenna Design Software. Accessed: Jan. 1, 2022. [Online]. Available: https://www.ticra.com/software /grasp/

[51] R. H. Clarke and J. Brown, "Diffraction Theory and Antennas," Ellis Horwood Limited. 1980.

Álvaro F. Vaquero (Member, IEEE) was born in Salinas, Spain, in 1990. He received the B.Sc., M.Sc., and PhD degrees in telecommunications engineering from the Universidad de Oviedo (UO), Gijón, Spain, in 2015, 2017, and 2021, respectively.

From 2016 to 2021, he was a Research Assistant with the Signal Theory and Communications Area, UO. He was a Visiting Researcher at the Antennas and Propagation Group, Instituto de Telecomuncações, Lisbon, Portugal, in 2017, 2021 and 2023. In December 2021, he joined the Department of Signals, Systems, and Radiocommunications, Group of Applied Electromagnetics, Universidad Politécnica de Madrid, Spain, as a Post-Doc Researcher involved in the development of reflective intelligent surfaces (RIS) for 5G/6G networks. He moved back to the University of Oviedo in 2022. In 2023, he was a recipient of a Post-doctoral Fellowship financed by the Spanish Government. He has authored more than 45 peer-reviewed journals and conference papers. His current research interest includes the development of efficient techniques for the analysis and optimization of spatially fed arrays, especially reflectarray, transmitarray, and metasurfaces for near- and far-field applications, the design of reconfigurable intelligent surfaces (RIS), and the design of additive manufacturing antennas in mm-wave frequencies.

Dr. Vaquero has also received the 2022 Outstanding Ph.D. Thesis Award from UO and the 2021 National Award for the Best Ph.D. Thesis on Telecommunication Engineering for 5G Innovation for Sustainable Connectivity. He was also recipient of the IEEE Antennas and Propagation Society Fellowship (APSF) in 2023.

Eduardo Martinez-de-Rioja (S'15–M'18) was born in Madrid, Spain. He received the Telecommunication Engineer and Ph.D. degrees from the Universidad Politécnica de Madrid (UPM), Madrid, in 2014 and 2018, respectively.

From 2015 to 2019, he was with the Applied Electromagnetics Group at UPM, as a Research Assistant. In 2016, he joined the Electrical and Computer Engineering Department, University of Toronto, Toronto, Canada, as a Visiting Ph.D. Student. Since 2019, he is an Assistant Professor at the Department of Signal Theory and Communications and Telematic Systems and Computing, Universidad Rey Juan Carlos, Madrid, Spain. His research interests include the design of advanced antenna systems based on reflectarrays, frequency selective surfaces and other planar quasi-periodic structures, for satellite communications and millimeter-wave 5G/6G applications.

Dr. Martinez-de-Rioja was a recipient of the 2019 National Awards of the Spanish Association of Telecommunication Engineers to the "Best Ph.D. Thesis" in the category of Government Satellite Services. He also received the "Young Researchers Award" in the XXXIII National Symposium of URSI, held in Granada, Spain (2018).

Manuel Arrebola (Senior Member, IEEE) was born in Lucena, Spain. He received the M.Sc. degree in telecommunication engineering from the University of Málaga, Málaga, Spain, in 2002, and the Ph.D. degree from the Technical University of Madrid (UPM), Madrid, Spain, in 2008.

From 2003 to 2007, he was a Research Assistant with the Department of Electromagnetism and Circuit Theory, UPM. He was a Visiting Researcher with the Department of Microwave Techniques, Universität Ulm, Ulm, Germany. In 2007, he joined the Department of Electrical Engineering, University of Oviedo, Gijón, Spain, where he is currently an Associate Professor with the Signal Theory and Communications Group. In 2009, he was with the European Space Research and Technology Center, European Space Agency, Noordwijk, The Netherlands, as a Visiting Researcher. He has been a Visiting Professor with several institutions, such as the Edward S. Rogers Sr. Department of Electrical and Computer Engineering, University of Toronto, Toronto, ON, Canada, in 2018; the Institute of Sensors, Signals and Systems, Heriot-Watt University, Edinburgh, U.K., in 2019; and the Antennas and Propagation Group, Instituto de Telecomuncações, Lisbon, Portugal, in 2023. He has authored and coauthored more than 200 peer-reviewed journals and conference papers. His current research interests include the application of innovative manufacturing techniques in mm and sub-mm-wave antenna design and the development of efficient analysis, design, and optimization techniques of spatial fed arrays, including reflectarrays and transmitarrays, and periodic structures for near- and far-field applications.

Dr. Arrebola was a co-recipient of the 2007 Sergei A. Schelkunoff Transactions Prize Paper Award from the IEEE Antennas and Propagation Society. He has also received the 2008 Outstanding Ph.D. Thesis Award from UPM and the 2009 National Award for the Best Ph.D. Thesis on Telecommunication Networks and Services. Since 2022, he has been an Associate Editor of the IEEE TRANSACTIONS ON ANTENNAS AND PROPAGATION and since 2024 he has been appointed as a Regional Delegate of the European Association on Antennas and Propagation (EurAAP).

José A. Encinar (Live Fellow, IEEE) was born in Madrid, Spain. He received the Electrical Engineer and Ph.D. degrees, both from Universidad Politécnica de Madrid (UPM), in 1979 and 1985, respectively.

Since January 1980, he has been with the Applied Electromagnetics Group at UPM, as a Teaching and Research Assistant from 1980 to 1982, as an Assistant Professor from 1983 to 1986, as Associate Professor from 1986 to 1991, and as Full Professor from 1991 to 2024, when he retired. From February to October of 1987, he was a Postdoctoral Fellow of the NATO Science

Program with the Polytechnic University, Brooklyn, NY, USA. He was a Visiting Professor with the Laboratory of Electromagnetics and Acoustics at Ecole Polytechnique Fédérale de Lausanne (EPFL), Switzerland, in 1996, and with the Institute of Electronics, Communication and Information Technology (ECIT), Queen's University Belfast, U.K., in 2006 and 2011. His research interests include numerical techniques for the analysis of multi-layer periodic structures, design of frequency selective surfaces, printed arrays and reflectarrays.

Prof. Encinar has co-authored more than 100 journal and 200 conference papers, one book and several book chapters, and he is co-inventor of ten patents. He received the "2005 H.A. Wheeler Applications Prize Paper Award" and the "2007 S.A. Schelkunoff Transactions Prize Paper Award" by IEEE Antennas and Propagation Society, and the "EuRAAP Antenna Award 2022" by the The European Association on Antennas and Propagation (EurAAP). He has been a member of the Technical Programme Comity of several International Conferences (EUCAP, ESA Antenna Workshops, Loughborough Antennas & Propagation Conference) and TPC chair of the 16th European Conference on Antennas and Propagation (EuCAP2022).

Maha Achour has more than 25 years' experience in leadership roles in the semiconductor, wireless RF, optical communications, sensing and defense industries – with both startup and public compan- ies. Recognized for her deep technology back- ground, management, and business development skills, Maha has been recently named to Forbes' "50 Over 50 – Vision" list of women who are suc- cessfully running companies and leading move- ments. Before founding Metawave, she served as co-founder and CEO of Polyceed-Dyenamics (where she serves now as Chair of the Board), co-founder and CTO of Rayspan, Director of Advanced Technology at SDRC (Boeing), Director of Advanced Technology at Optical Access, and lead System Engineer at Tiernan Comm where she worked on first broadcast HDTV-over satellite sys- tem. She has also led various DARPA projects in advanced wireless MIMO and optical device technologies. A sought-after industry speaker and thought leader, Maha holds a doctorate degree in physics from the Massachusetts Institute of Technology (MIT). She has authored more than 35 publications, holds more than 75 granted patents, and has more than 150 pending patent applications.